The Matsuno-Gill model on the sphere

Ofer Shamir[1], Chaim I. Garfinkel[2], Edwin P. Gerber[1] and Nathan Paldor[2]†

[1]Courant Institute of Mathematical Sciences, New York University, New York, New York

[2]Fredy and Nadine Herrmann Institute of Earth Sciences, Hebrew University of Jerusalem, Edmond J. Safra Campus, Givat Ram, Jerusalem, 91904, Israel

(Received xx; revised xx; accepted xx)

We extend the Matsuno-Gill model, originally developed on the equatorial β-plane, to the surface of the sphere. While on the β-plane the non-dimensional model contains a single parameter, the damping rate γ, on a sphere the model contains a second parameter, the rotation rate $\epsilon^{1/2}$ (Lamb number). By considering the different combinations of damping and rotation we are able to characterize the solutions over the $(\gamma, \epsilon^{1/2})$ plane. We find that the β-plane approximation is only accurate for fast rotation rates, compared to the time on which gravity waves propagate around the sphere, while the particular solution studied by Matsuno and Gill is only accurate for fast rotation and moderate damping rates, where the relaxation time is comparable to the time on which gravity waves propagate around the sphere. Other regions of the parameter space can be described by different approximations, including radiative relaxation, geostrophic, weak temperature gradient, and non-rotating limits. The effect of the additional parameter introduced by the sphere is to alter the eigenmodes of the free system. Thus, unlike the solutions obtained by Matsuno and Gill, where the long-term response to a symmetric forcing consists solely of Kelvin and Rossby waves, the response on the sphere includes other waves as well, depending on the combination of γ and $\epsilon^{1/2}$. The Matsuno-Gill model in its original formulation applies to Earth's oceans, and to some extent the β-plane applies to Earth's troposphere. In Earth's stratosphere, or in Venus or Titan, only the spherical formulation applies.

Contents (for review purposes)

† Email address for correspondence: nathan.paldor@mail.huji.ac.il

1. Introduction

One of the pillars of tropical meteorology is the Matsuno-Gill model, which provides a simple, yet informative, description of the circulation patterns in the tropics using the framework of the forced-dissipated Rotating Shallow Water Equations (RSWEs). The model is named after the seminal works of Matsuno (1966) and Gill (1980) who studied these equations on the infinite equatorial β-plane and obtained steady-state solutions in response to heating that is meridionally-variable (i.e., the Hadley circulation) and zonally-asymmetric (i.e., the Walker circulation) subject to linear damping (i.e., Rayleigh friction) and thermal relaxation (i.e., Newtonian cooling).

While studying "quasi-geostrophic" motions in the equatorial area, Matsuno obtained explicit expressions for the frequencies and latitude-dependent amplitudes of zonally propagating wave solutions of the (free) RSWEs on the infinite equatorial β-plane by solving for the eigenvalues and corresponding eigenfunctions of the associated eigenvalue problem (Matsuno 1966). Using those eigen-solutions, Matsuno then obtained the spatial distribution of forced stationary waves for general forms of forcing (provided they can be spanned by the eigenfunctions) and examined the particular response to a (stationary) Kelvin wave mass source/sink (the first eigen-solution of the free RSWEs). For small dissipation rates, the resulting surface-elevation consists of equatorially symmetric ridges and troughs that straddle the equator, and were described by Matsuno as the "petals" of a flower (Fig. 9 in Matsuno 1966, rendition in Fig. 1 of the present work). Inspired by Matsuno's imagery, and considering the prevalence of this pattern in tropical meteorology, we refer to it as "La Fleur-de-lis" after the iconic emblem. Carrying on this analogy, the prevailing winds in this case parallel the stem along the equator until reaching the convergence/divergence zones situated at the ovaries. Physically, the resulting flow pattern can be explained in terms of geostrophic adjustment to a mass source introduced into a quiescent state.

Likewise, while studying the heat-induced tropical circulation, Gill used the forced-dissipated RSWEs on the infinite equatorial β-plane (under the long-wave approximation) to study the stationary circulation patterns in response to a zonally localized heat source (with respect to an infinite zonal domain) with a geopotential forcing corresponding to Kelvin and Mixed Rossby Gravity (MRG) waves (the first and second eigen-solutions of the free RSWEs, respectively) (Gill 1980). A key feature of Gill's analysis is the description of the steady circulation in terms of the constituent waves. For small dissipation rates, the response to symmetric heating about the equator consists of a westward propagating Rossby wave and an eastward propagating Kelvin wave. The former manifests as off-equatorial pressure cells corresponding to the petals of La Fleur-de-lis, while the latter manifests as an elongated equatorial pressure cell corresponding to the stem. The response to anti-symmetric heating about the equator consists of a westward propagating MRG wave and an eastward propagating Inertia Gravity (IG) wave. The combination of the two is manifested by an off-equatorial pressure dipole centered to the west of the forcing and elongated westward. Gill then studied more general forcings as a combination of these former two cases.

Since its formulation, the Matsuno-Gill model was proven useful for understanding most major tropical phenomena. In the context of the Madden-Julian-Oscillation, the same analysis used by Gill for finding the steady-state responses was used to find the transient response to an easterly moving heat source mimicking a moving convective region, but for a frame of reference that travels with the heat source (Chao 1987; Biello & Majda 2005; Majda & Stechmann 2009; Sobel & Maloney 2012; Adames & Kim 2016; Kacimi & Khouider 2018). In the context of the Intertropical Convergence Zone (ITCZ), a

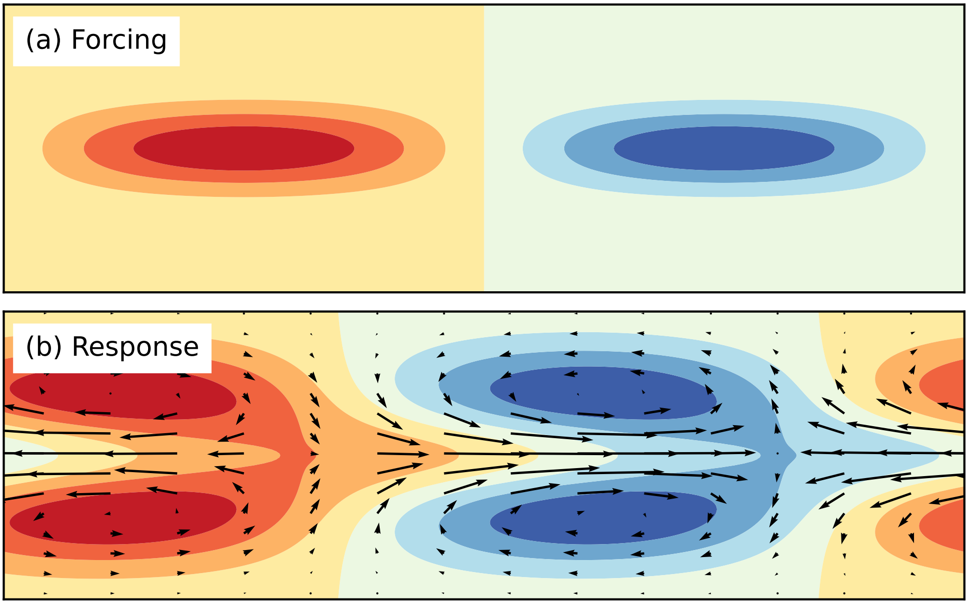

Figure 1. **La Fleur-de-lis on the β-plane:** Rendition of figure 9 in Matsuno (1966). (a) The mass source/sink. (b) The steady-state geopotential (color shading) and winds (arrows). Contours range from -1 to 1 every 0.25.

zonal running mean of Gill's solutions was used to study the co-location of the rainbands and low-level westerlies (Chao & Chen 1999). The Matsuno-Gill model with a Bjerknes feedback was used to study the double ITCZ (Adam 2018), and the model was also used to study the effects of eastern Pacific El Niño and central Pacific El Niño on the ITCZ (Zhu *et al.* 2018). In the context of equatorial superrotation, it was shown that the Matsuno-Gill model does not exhibit equatorial superrotation due to an inconsistent parameterization of vertical momentum transfer in the model (Showman & Polvani 2010). The model was also used to interpret momentum flux patterns in the transition to strong equatorial superrotation (Arnold *et al.* 2012). Lutsko (2018) studied the response to diabatic heating in idealized, dry general circulation model and found that equatorial superrotation is associated with the breakdown of the linear regime where the Matsuno-Gill solutions apply. The Matsuno-Gill model was also used as a prototype model for studying the weak temperature gradient approximation, where it was shown that under this approximation the Rossby wave part of the response is not equatorially trapped and the model has a far-field response to a localized tropical heating (Bretherton & Sobel 2003). Finally, the Matsuno-Gill model has recently been applied in the study of stratospheric chemistry (Wilka *et al.* 2021).

Physically, for the Matsuno-Gill model to be relevant, the temporal variations of the forcing need to be slow compared to the relaxation time of the atmosphere, such that the steady-state solutions are applicable. In addition, the meridional extent of the forcing needs to be sufficiently small so that the response may be described using the β-plane approximation. In Matsuno's words (paraphrasing to remove equation numbers and nomenclature):

> "It may be plausible to assume that external forces or inhomogeneous terms are not zero only in the finite distance from the equator".

However, one can think of long-term forcing on Earth with global-scale meridional extents. For example, atmospheric stationary waves forced by asymmetries in the lower boundary, such as topography, ocean-heat fluxes, and land-sea contrast. Certainly, the meridional extent of all three forcing is global, and their temporal variations are slow compared to the relaxation time of the atmosphere. One can also consider the response to long-term radiative forcing at the top of the atmosphere. For example, the annually averaged net radiative forcing varies in the meridional direction as a cosine of the latitude from about +75 W m^{-2} (heating) at the equator to -100 W m^{-2} (cooling) at the poles. A final example is the steady-state response to aerosol-induced stratospheric heating (surface cooling) following volcanic eruptions. The typical lifespan of aerosols in the stratosphere is about a year, long compared to the relaxation time of their induced radiative forcing, and their spatial coverage in some major events can be substantial. For example, the meridional extent of the aerosol-induced heating following the 1991 Mt. Pinatubo eruption extended from about $-45°$S to $45°$N (Toohey *et al.* 2014; DallaSanta *et al.* 2019). The global dynamical response to these external forcing cannot be fully described by a theory limited to the equatorial β-plane.

Mathematically, the analyses by Matsuno (1966) and Gill (1980) were greatly simplified by the fact that the free non-dimensional RSWEs on the infinite equatorial β-plane can be made parameter-free. In contrast, the free RSWEs on the sphere can only be reduced to a single non-dimensional parameter, referred to as Lamb number and denoted here by $\epsilon = (2\Omega a)^2/gH$ (where a, g and Ω denote the mean radius, gravitational acceleration and angular frequency of the celestial body in question, and H denotes the mean layer thickness of the layer of fluid in question). In addition, the analyses by Matsuno (1966) and Gill (1980) were also simplified by the availability of exact analytic solutions for the free RSWEs on the infinite equatorial β-plane. However, on the sphere there are only approximate solutions in the limits of small and large ϵ. Specifically, as discussed in Garfinkel *et al.* (2017) the free RSWEs on the infinite equatorial β-plane approximate the free RSWEs on the sphere in the limit $\epsilon \to \infty$, but only to zero-order in $\epsilon^{-1/4}$. More accurate approximations in this limit were obtained by De-Leon & Paldor (2011). Like the infinite equatorial β-plane, the meridional part of the solutions obtained by De-Leon & Paldor (2011) correspond to the Hermite functions, but of a scaled latitude (similar results were obtained by Longuet-Higgins (1968), albeit only for zonal wavenumbers of order 1). In the opposite limit, as $\epsilon \to 0$, the free RSWEs on the sphere can be approximated to zero-order in $\epsilon^{1/2}$ by the non-rotating Shallow Water Equations, where the meridional part of the solutions are described by the associated Legendre polynomials. Higher order approximations were obtained by Hough (1897, 1898) and Longuet-Higgins (1968). In fact, the problem of forced oscillations of infinitely long period (i.e., stationary solutions) in the RSWEs on the sphere is also studied in Hough (1897), but without dissipation. In addition, Paldor *et al.* (2013) obtained simpler expression using Gegenbauer functions to approximate the meridional part of the solutions in this limit.

The value of the Lamb number on Earth varies by 4 orders of magnitude from $\epsilon = 10$, corresponding to a gravity wave speed of 300 ms^{-1} associated with the barotropic mode in the atmosphere (Fritts & Alexander 2003), to $\epsilon = 10^5$ corresponding to a gravity wave speed of 3 ms^{-1} associated with the first baroclinic mode in the oceans (Chelton *et al.* 1998). Hence it is not clear whether the asymptotic solutions (either $\epsilon \to 0$ or $\epsilon \to \infty$) from these earlier works are relevant for the response to a Matsuno-Gill like forcing on the sphere. In addition, Gill studied the response to a dissipation rate, denoted here by γ, corresponding to a relaxation time of about 2 days. However, the typical relaxation time of the atmosphere varies by at least 1 order of magnitude, from $O(1)$ to $O(10)$ days, and is difficult to constrain by observations. Finally, on celestial bodies that rotate slower than Earth, for example, Venus and Titan, erstwhile equatorial wave modes are observed to extend well into midlatitudes (Svedhem *et al.* 2007; Mitchell *et al.* 2011; Yamamoto 2019; Peralta *et al.* 2020), limiting the relevance the β-plane solutions.

The ubiquity of the Matsuno-Gill model in the study of the Tropics, the existence of large-scale, long-term, forcing on Earth, and the dependence of the β-plane approximation on Lamb number, all motivate the study of the Matsuno-Gill model on the sphere. Specifically, a key feature of the present work is the analysis of the Matsuno-Gill model on the sphere in the $(\gamma, \epsilon^{1/2})$ plane.

The manuscript is organized as follows: In section 2 we introduce the governing equations, and provide some general considerations employed in the subsequent sections. In section 3 we describe the suitable choice of the applied forcing in order to extend the original works of Matsuno and Gill. In section 4 we described numerically obtained solutions of the Matsuno-Gill model on the sphere in representative cases. In section 5 we describe some "simple solutions of the heat induced circulation", and their applicability to Earth, Venus, and Titan in section (6). In section 7 we examine the wave composition of the response in the Matsuno-Gill model on the sphere. In section 8 we examine the response to a localized forcing (both zonally and meridionally) akin to that used by Gill. Finally, the results are summarized and discussed in section 9.

2. Governing equations and preliminary considerations

The Matsuno-Gill model describes steady-state wave-solutions of the forced-dissipated, Rotating Shallow Water Equations (RSWEs). In their original works, Matsuno (1966) and Gill (1980) obtained exact analytic solutions of the linearized version of these equations on the infinite equatorial β-plane for particular forms of forcing and dissipation terms. We extend the Matsuno-Gill model to the surface of the sphere, using the same forms of forcing and dissipation. In particular, following Matsuno and Gill, we assume that:

(i) There is no momentum forcing, only a prescribed "heat/mass" source added to the continuity equation. The extension of the forcing used by Matsuno and Gill to the sphere is described in more details in section 3.

(ii) We let the dissipative terms in the momentum equations and the continuity equation take the forms of Rayleigh friction and Newtonian cooling, respectively, and assume that they can all be characterized by the same time scale. While such forms of dissipation are likely not the most suitable ones for any particular application, as noted by Gill (1980), they are the simplest.

Let a, g and Ω denote the mean radius, gravitational acceleration and angular frequency of the celestial body in question, and let H denote the mean layer thickness of the layer of fluid in question. Then, using a as the horizontal length scale, and $\sqrt{a^2/gH}$ as the time scale (which implies that $\sqrt{gH}$ is the horizontal velocity scale), the linearized forced-dissipated (time-dependent) RSWEs in spherical coordinates can be written in a non-dimensional form as follows

$$\frac{\partial u}{\partial t} - \epsilon^{1/2} v \sin\phi + \frac{1}{\cos\phi}\frac{\partial \Phi}{\partial \lambda} = -\gamma u \tag{2.1a}$$

$$\frac{\partial v}{\partial t} + \epsilon^{1/2} u \sin\phi + \frac{\partial \Phi}{\partial \phi} = -\gamma v \tag{2.1b}$$

$$\frac{\partial \Phi}{\partial t} + \frac{1}{\cos\phi}\left[\frac{\partial u}{\partial \lambda} + \frac{\partial}{\partial \phi}(v\cos\phi)\right] = -\gamma\Phi + Q, \tag{2.1c}$$

where t denotes time; $0 \leqslant \lambda < 2\pi$ and $-\pi/2 \leqslant \phi \leqslant \pi/2$ denote the longitudinal and latitudinal angles; u and v denote the zonal and meridional velocity components; Φ denotes the geopotential height anomaly (where the non-dimensional mean geopotential equals 1); $\gamma > 0$ denotes the damping/cooling coefficient; $Q = Q(\lambda, \phi)$ is a prescribed forcing (meaning that Q is a known function of the longitude and latitude); and ϵ is Lamb number defined by

$$\epsilon = (2\Omega a)^2/gH. \tag{2.2}$$

Based solely on the different ways of grouping its constituent parameters, Lamb number can be interpreted in a number of ways. Depending on the appropriate length and time scale in a particular application, $\epsilon^{1/2}$ may play the role of the (inverse) Rossby number or the Froude number. Instead, Lamb number is more consistently interpreted based on its location in the equations, and not based on its constituent parameters. Thus, under the preset scaling, where $\epsilon^{1/2}$ appears in front of the Coriolis terms in the momentum equations, it plays the role of the non-dimensional rate of rotation (measured relative to the time over which a gravity wave can appreciably propagate around the sphere).

The validity of the linearization depends on both the amplitude and the spatial variability of the forcing. For highly oscillating Q the resulting u, v, Φ fields can also be highly oscillating and the advection terms can be non-negligible even for small forcing amplitude. In the present work, we take the term "the Matsuno-Gill model" to mean the linearized equations, so only low Fourier modes should be considered. In practice, the forcing can often be treated as slowly varying, e.g. for the purpose of providing simple descriptions of the Hadley and Walker circulations. Yet, the validity of the linearization should be confirmed on a per-case basis, and the problem of non-linear adjustment of the forced-dissipated RSWEs merits additional study.

The stationary system is obtained by setting $\partial/\partial t$ equal to zero in system (2.1), yielding

$$\boxed{\begin{aligned} -\epsilon^{1/2} v \sin\phi + \frac{1}{\cos\phi}\frac{\partial \Phi}{\partial \lambda} &= -\gamma u && (2.3a)\\ \epsilon^{1/2} u \sin\phi + \frac{\partial \Phi}{\partial \phi} &= -\gamma v && (2.3b)\\ \frac{1}{\cos\phi}\left[\frac{\partial u}{\partial \lambda} + \frac{\partial}{\partial \phi}(v\cos\phi)\right] &= -\gamma \Phi + Q, && (2.3c) \end{aligned}}$$

which we shall refer to as the Matsuno-Gill model on the sphere. Aside from some trivial changes associated with the choice of scaling and the spherical geometry this is precisely the fundamental system studied in the planar versions of the model, i.e. system (30) of Matsuno (1966) and equations (2.6)-(2.8) of Gill (1980). Note, however, that Gill subsequently imposed the longwave approximation, which is tantamount to neglecting $-\gamma v$ on the RHS of (2.3*b*).

Before continuing, we introduce one further simplification. Observe that the coefficients of the Matsuno-Gill model (2.3) are λ-independent. Thus, we may replace each λ-dependent quantity with a Fourier series in λ and consider each Fourier mode separately. Specifically, we assume that the forcing Q and the unknowns u, v, Φ all have the form:

$$\xi(\lambda, \phi) = \sum_{m=-\infty}^{\infty} \xi^m(\phi) \exp(im\lambda), \tag{2.4}$$

where $\xi = \{u, v, \Phi, Q\}$ and $\xi^m(\phi)$ is the corresponding latitude-dependent coefficient.

The resulting system for each individual Fourier mode m is then

$$-\epsilon^{1/2} v^m \sin\phi + \frac{im}{\cos\phi}\Phi^m = -\gamma u^m \tag{2.5a}$$

$$\epsilon^{1/2} u^m \sin\phi + \frac{d\Phi^m}{d\phi} = -\gamma v^m \tag{2.5b}$$

$$\frac{1}{\cos\phi}\left[imu^m + \frac{d}{d\phi}(v^m\cos\phi)\right] = -\gamma\Phi^m + Q^m. \tag{2.5c}$$

Similarly, Matsuno assumed a zonally periodic forcing and studied the latitude-dependent boundary value problem remaining after a Fourier decomposition in the zonal direction. In contrast, Gill assumed a zonally localized (aperiodic) forcing and studied the longitude-dependent problem remaining after expanding the latitudinal part in terms of the eigen-solutions of the free problem. In section 8 we show how the solutions of (2.5) combine to yield the response to a localized-forcing akin to the one used by Gill.

A key property of the free RSWEs on the sphere is the existence of two qualitatively different solution-regimes: an equatorial regime, in which the solutions are non-negligible only in the vicinity of the equator (i.e., equatorially trapped solutions), and a global regime, in which the solutions are non-negligible at all latitudes. Generally speaking, the former is realized in the limit of large Lamb number, while the latter is realized in the limit of small Lamb number. More accurately, as noted in Boyd & Zhou (2008) and Boyd (2018), for a given Lamb number the equatorial regime is also realized in the limit of large zonal wavenumber. However, as discussed above, the linearization may no longer be applicable if the solutions have appreciable power at high Fourier modes, and in the context of the Matsuno-Gill model we are only concerned with low Fourier modes.

The free problem consists of finding the dispersion relations and latitude-dependent amplitudes of zonally propagating waves, i.e. solutions of the form

$$\{u(t,\lambda,\phi), v(t,\lambda,\phi), \Phi(t,\lambda,\phi)\} = \{u^m(\phi), v^m(\phi), \Phi^m(\phi)\}\exp[i(m\lambda - \omega t)], \tag{2.6}$$

where ω is the wave-frequency. Setting $\gamma = 0$ and $Q = 0$ in (2.1) and substituting (2.6) yields the following eigenvalue problem for each Fourier mode m of the free waves

$$\mathcal{L}X = i\omega X, \tag{2.7}$$

where

$$\mathcal{L} = \begin{bmatrix} 0 & -\epsilon^{1/2}\sin\phi & \dfrac{im}{\cos\phi} \\ \epsilon^{1/2}\sin\phi & 0 & \dfrac{d}{d\phi} \\ \dfrac{im}{\cos\phi} & (\dfrac{d}{d\phi} - \tan\phi) & 0 \end{bmatrix}, \quad X = \begin{bmatrix} u^m \\ v^m \\ \Phi^m \end{bmatrix}. \tag{2.8}$$

Formally, the above equation is equivalent to the Matsuno-Gill model (2.5) with $\omega = i\gamma$ (and $Q = 0$). However, the two problems are different in essence. The free problem consists of an eigenvalue problem where ω is the unknown eigenvalue(s), while the dissipated problem consists of a boundary value problem for given (i.e., known) values of γ.

3. The prescribed forcing

Before comparing solutions of the Matsuno-Gill model on the equatorial β-plane with those on the sphere, we first ensure that the two converge in the appropriate limit. As was shown in Garfinkel *et al.* (2017), for any fixed zonal wavenumber, free RSWEs on the equatorial β-plane approximate free RSWEs on the sphere in the limit $\epsilon \to \infty$. Consider the relation $\omega = i\gamma$ between the frequency ω in solutions of the free system and the dissipation γ in the steady-state system. For the two systems to converge, the prescribed forcing must also be identical, which guides the following choices.

Starting with the latitudinal dependence, the forcing used by Matsuno and Gill (the latter only in response to a symmetric forcing) in the continuity equation corresponds to the geopotential height field of a Kelvin wave on the equatorial β-plane. Hence, a natural extension of the forcing is the geopotential height field corresponding to the "Kelvin" wave on the sphere. The existence of a (nearly) non-dispersive wave that converges to the equatorial Kelvin wave on the β-plane for $\epsilon \to \infty$ was verified in Garfinkel *et al.* (2017). From the point of view of the eigenvalue problem associated with the free RSWEs on the sphere, however, this wave is more accurately classified as the lowest mode eastward IG wave. Likewise, the forcing used by Gill in the continuity equation in response to a meridionally anti-symmetric heating corresponds to the geopotential height field of an equatorial MRG wave. Hence, a natural extension to the present work is the geopotential height field corresponding to the MRG wave on the sphere, whose existence was verified in Paldor *et al.* (2018).

Next, with regard to the longitudinal dependence, as discussed in section (2) we may consider each Fourier mode separately. Hence, without loss of generality we assume that the forcing consists of a single Fourier mode and study the response to the representative case of $m = 5$. This value is specifically chosen in order to reproduce Matsuno's solutions for large values of ϵ (fast rotation). Specifically, the results presented in Figure 9 of Matsuno (1966) (Fig. 1 of the present work) were obtained using a planar (non-dimensional) wavenumber $k = 0.5$. The spherical wavenumber of the present work is related to the latter by $m = \epsilon^{1/4}k$. Hence, $k = 0.5$ corresponds to $m = 5$ for $\epsilon = 10^4$, which is used throughout this work as a representative value for the large ϵ limit. Due to the periodicity of the spherical coordinate system, m takes only integer values and hence particular values of k correspond to acceptable values of m only for certain values of ϵ. The response to a wavenumber 1 forcing is qualitatively different from all other wavenumbers $m > 1$ in that the regular solutions of (2.5) have non-vanishing velocities at the poles, and is left for the supplementary material. The case $m = 0$ requires special treatment and is of lesser interest in the context of the Matsuno-Gill model, which is concerned with zonally asymmetric forcing.

4. Representative solutions

In the absence of exact analytic solutions for the Matsuno-Gill model on the sphere for arbitrary values of γ and $\epsilon^{1/2}$, numerical approximations can be readily obtained. In the present work, we use a Chebyshev collocation method (e.g. Trefethen 2000) to solver (2.5) as follows. For each wavenumber m, we first solve the eigenvalue problem associated with zonally propagating wave solutions of the free RSWEs to obtain the latitude-dependent amplitudes of the Kelvin and MRG waves. For any value of $\epsilon^{1/2}$, the Kelvin wave can be identified as the first wave with $\omega > m$ (assuming $m > 0$ by convention, Garfinkel *et al.* 2017). In contrast, the identification of the MRG wave depends on the value of $\epsilon^{1/2}$. The point where the MRG transitions from an IG wave at small wavenumbers to a Rossby wave at large wavenumbers is $m^{\star} = \epsilon^{1/4}/\sqrt{2}$ (Paldor *et al.* 2018). For $m < m^{\star}$, the MRG is identified as the first wave with $-\omega > m$, while for $m > m^{\star}$, it is identified as the first wave with $-\omega < m$ (assuming $m > 0$ by convention). Having solved for the Kelvin and MRG waves, we then substitute the resulting geopotential height for Q^m and solve

	Light damping	Moderate damping	Heavy damping
Fast rotation	**LF** $(10^{-2}, 10^{2})$	**MF** $(1, 10^{2})$	**HF** $(10^{2}, 10^{2})$
Moderate rotation	**LM** $(10^{-2}, 1)$	**MM** $(1, 1)$	**HM** $(10^{2}, 1)$
Slow rotation	**LS** $(10^{-2}, 10^{-2})$	**MS** $(1, 10^{-2})$	**HS** $(10^{2}, 10^{-2})$

Table 1. Particular values of the $(\gamma, \epsilon^{1/2})$ plane used throughout the study. For the sake of brevity, we denote the different combinations using a two-letter acronym where the first letter corresponds to one of the three rates of damping and the second letter to one of the three rates of rotation, e.g. LF denotes the case of Light damping and Fast rotation.

the boundary value problem associated with the Matsuno-Gill model (2.5). For the sake of simplicity, we normalize the prescribed forcing by its global absolute maximum, i.e. $\max_\phi |Q^m|$. In general, this choice could be inconsistent with the linearization but has no implications in the present work, where the system of equations is linearized from the outset.

We provide an overview of the numeric approximations in representative cases. As detailed in section 3, we choose wavenumber 5 as a representative wavenumber, which corresponds to the value used by Matsuno for the planar wavenumber $k = 0.5$ at $\epsilon^{1/4} = 10$. The results were verified qualitatively for wavenumbers 2, 8, and 1 (figures 1-6 in the supplementary material). The case $m = 1$ is qualitatively different from all other wavenumbers $m > 1$ in that the regular solutions of (2.5) have non-vanishing velocities at the poles (sections 2 and 3 in the supplementary material).

To sample the $(\gamma, \epsilon^{1/2})$ plane, we examine the 9 combinations of light/moderate/heavy damping, and slow/moderate/fast rotation. The particular values of γ and $\epsilon^{1/2}$ used throughout this study to represent these regimes are summarized in table 1. Recall that our time scale is $\sqrt{a^2/gH}$. Thus, under the present scaling, the damping and rotation rates are measured relative to the time taken for a gravity wave with speed $\sqrt{gH}$ to propagate the distance a. For example, "fast rotation" implies that the celestial body revolves around itself well before a gravity wave can travel a radial distance. Similarly, light damping implies that a gravity wave will propagate around the sphere before being appreciably damped. This differs from Matsuno's scaling, where time is scaled on the equatorial Rossby deformation time, and "light" damping implies that a gravity wave will propagate "far enough" to feel the effects of rotation before being appreciably damped.

As detailed in section 5.1, the conversion between the damping in Matsuno's scaling, denoted here by α, and the present scaling is $\alpha = \epsilon^{-1/4}\gamma$. Thus, for $\epsilon^{1/4} = 10$ (where the equatorial β-plane is found to be accurate), $\gamma = 10^{-2}$ (our light damping) correspond to $\alpha = 10^{-3}$, and $\gamma = 10^{2}$ (our heavy damping) correspond to $\alpha = 10^{1}$. Equivalently, for the same value of ϵ, Matsuno's damping rate $\alpha = 0.2$ corresponds to $\gamma = 2$, i.e., moderate damping in the present scaling.

Figures 2 and 3 provide representative solutions of the Matsuno-Gill model on the sphere in response to a (symmetric) Kelvin and an (anti-symmetric) MRG wave-5 forcing, respectively. The columns show different variables, the rows different combinations of γ and $\epsilon^{1/2}$. The meridional domain in each of these figures extends from the south pole to the north pole. For optimal presentation, the longitudinal domain corresponds to 1 zonal period ($2\pi/5$). In addition, each panel is normalized on its global absolute maximum, indicated within the white textbox at the bottom of each panel.

Our first observation from the representative solutions in figures 2 and 3 is that both equatorial and global solution-regimes are found across the $(\gamma, \epsilon^{1/2})$ plane. The solutions transition from equatorial at fast rotation rates to global at moderate or slow rotation rates, regardless of the damping rate. Accordingly, for the Matsuno-Gill model on the equatorial β-plane to approximate solutions on the sphere, the celestial body in question must be rapidly rotating. Indeed, looking at the response to a Kelvin wave-5 forcing in Fig. 2, we identify the Fleur-de-lis in the geopotential height field in the second row with moderate damping (red square). Figure 4 zooms in on the prescribed forcing (a) and geopotential height (b) obtained numerically (shadings), compared to the analytic solutions obtained by Matsuno (contours): our forcing yields solutions that converge to Matsuno's, confirming it as a natural extension of the latter. Likewise, Fig. 5 zooms in on the zonal (a) and meridional (b) winds obtained numerically (shadings), compared to Matsuno's solutions (contours). Clearly, the Fleur-de-lis on the sphere converges to the Fleur-de-lis on the β-plane, but only when the gravity wave propagation timescale is small relative to rotation and comparable to the damping. In all other cases, we obtain substantially different solution patterns.

Our second key take-away from the representative solutions concerns the balance of the forcing. For light damping (regardless of rotation rate), the divergence is identical to the applied forcing. From (2.5), for light damping the dissipation term is negligible compared to the forcing in the continuity equation, leaving only the divergence to balance the forcing. As the damping increases, the divergence remains spatially similar to the forcing (except for moderate-to-heavy damping and fast rotation), but it is orders of magnitude smaller. From (2.5), with heavy damping the forcing in the continuity equation is now balanced by the dissipation term. This is confirmed in the third, sixth, and ninth rows from the top of Figs. 2 and 3 (our heavy damping rate is $\gamma = 10^2$, table 1). Note that the weak divergence with heavy damping follows from the low amplitudes of the winds. While negligible, it is never identically zero. This is in contrast to purely two-dimensional flows, where the zonal divergence and meridional divergence compensate each other, so the total divergence is identically zero.

Our third observation from the representative solutions is the emergence of a geostrophic balance between the geopotential height field and the zonal and meridional wind fields at light damping and fast-to-moderate rotation rates (first and fourth rows from the top). From (2.5), the dissipation term becomes negligible for light damping, leaving the Coriolis and pressure-gradient terms to balance. Global-scale geostrophic balance is attainable by maintaining a vanishing geopotential height gradient at the equator (for $m > 0$ this implies that $\Phi = 0$ along the equator). For slow rotation rates, the Coriolis term is also small and the dissipation term cannot be neglected, explaining the lack of geostrophic balance. To a lesser extent (only outside the equator), the response at moderate damping and fast rotation rate (second row from the top) is also in near geostrophic balance, consistent with Matsuno's observation. In all other combinations of γ and $\epsilon^{1/2}$, the solutions are qualitatively far from geostrophic.

5. "Some simple solutions for heat-induced circulation" (paraphrasing Gill)

In the spirit of Gill (1980), we obtain approximate solutions of the "heat-induced" circulation of the Matsuno-Gill model on the sphere in special cases, including the β-

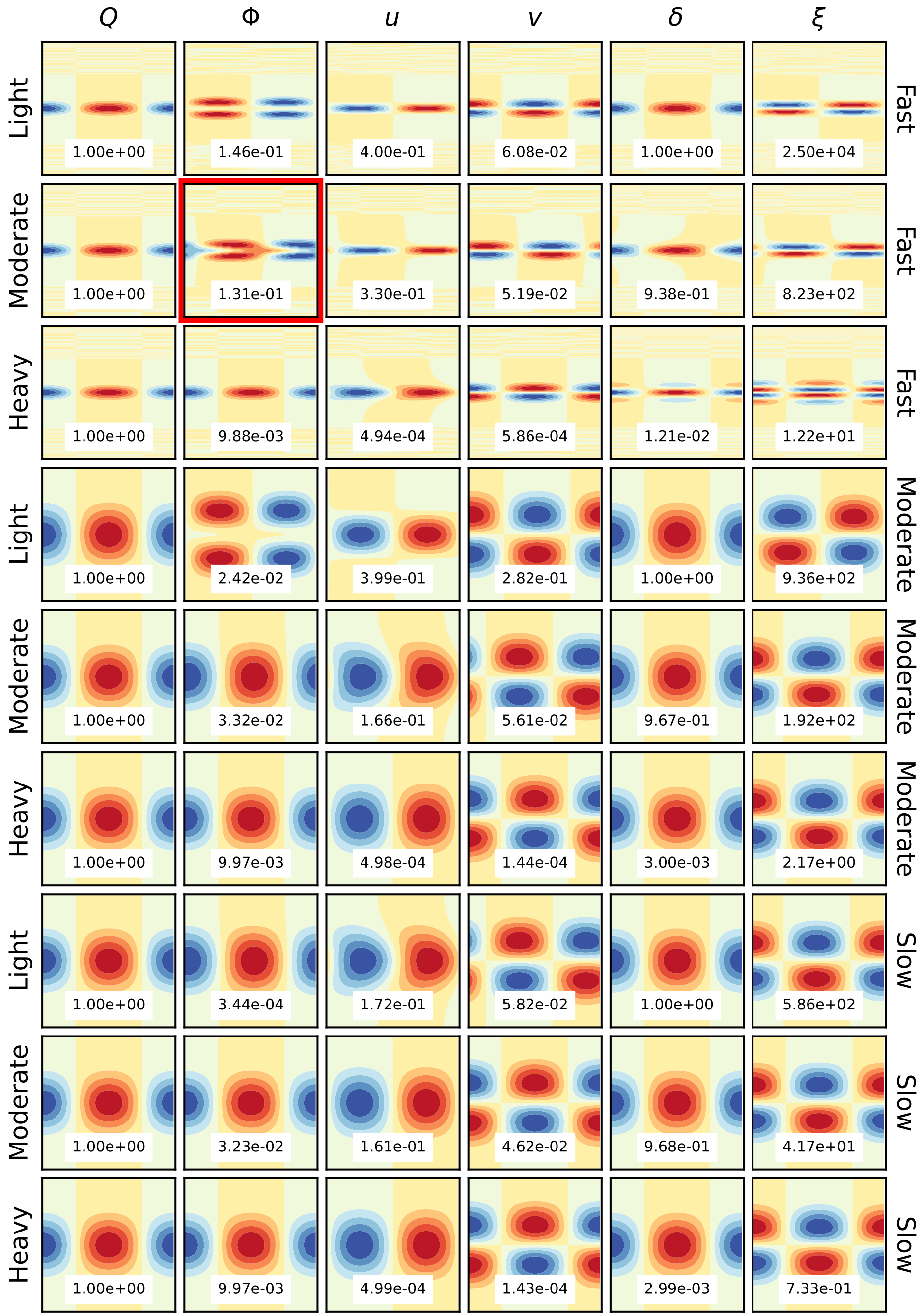

FIGURE 2. Steady-state response to a symmetric **Kelvin wave-5** forcing. In order from left to right: the prescribed forcing, the geopotential height, the zonal wind, the meridional wind, the divergence, and vorticity. The different rows correspond to the different samples of $(\gamma, \epsilon^{1/2})$ plane summarized in table 1. The damping and rotation rates for each case (row) are labeled on the left and right edges, respectively. The meridional domain in each panel extends from the south pole to the north pole. For the sake of clarity, the longitudinal domain in each panel corresponds to 1 zonal period. Contours range from -1 to 1 every 0.25. For the sake of presentation, each panel is normalized on its global absolute maximum, given in white text boxes.

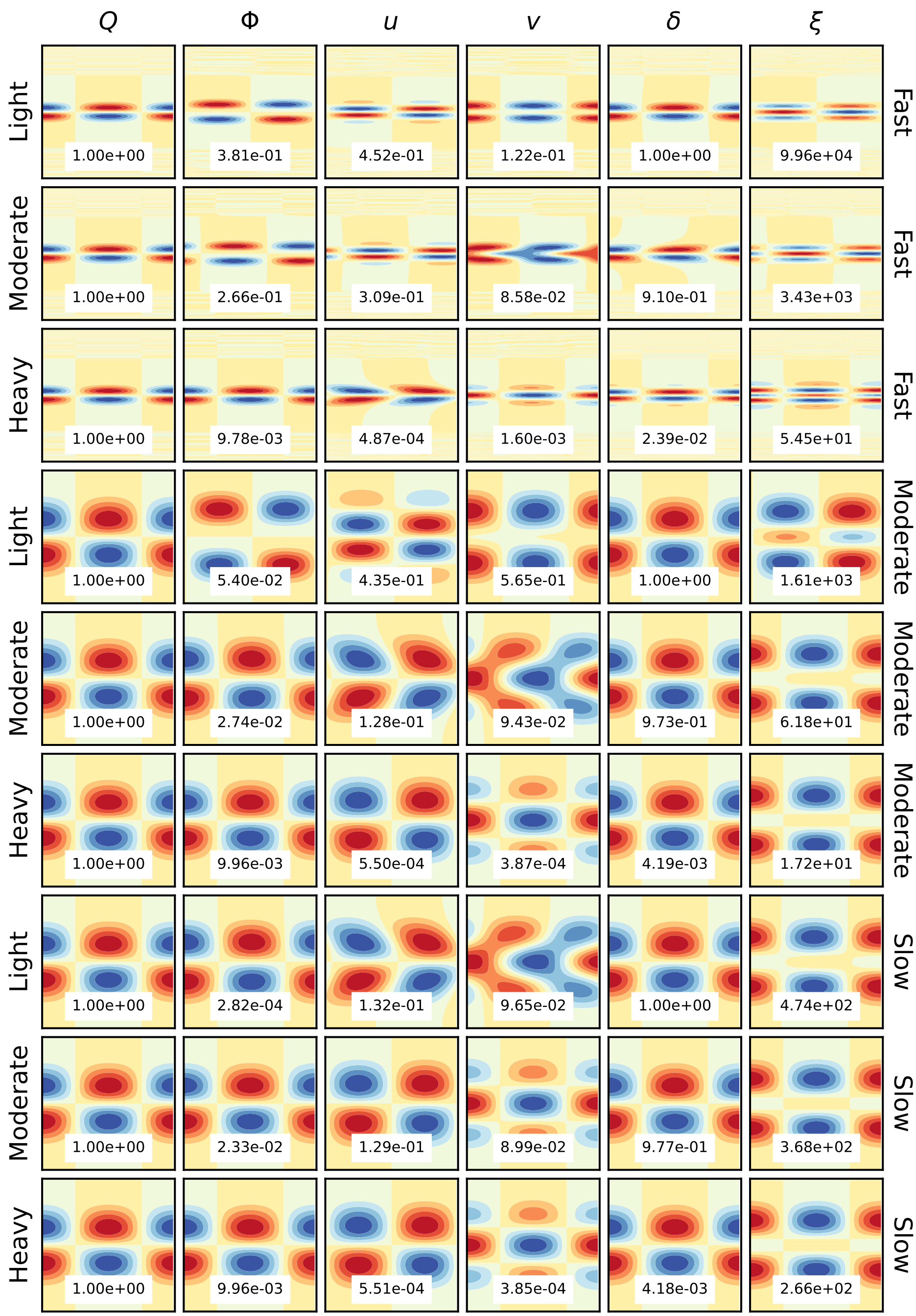

FIGURE 3. Steady-state response to a anti-symmetric **MRG wave-5** forcing. In order from left to right: the prescribed forcing, the geopotential height, the zonal wind, the meridional wind, the divergence, and vorticity. The different rows correspond to the different samples of $(\gamma, \epsilon^{1/2})$ plane summarized in table 1. The damping and rotation rates for each case (row) are labeled on the left and right edges, respectively. The meridional domain in each panel extends from the south pole to the north pole. For the sake of clarity, the longitudinal domain in each panel corresponds to 1 zonal period. Contours range from -1 to 1 every 0.25. For the sake of presentation, each panel is normalized on its global absolute maximum, given in white text boxes.

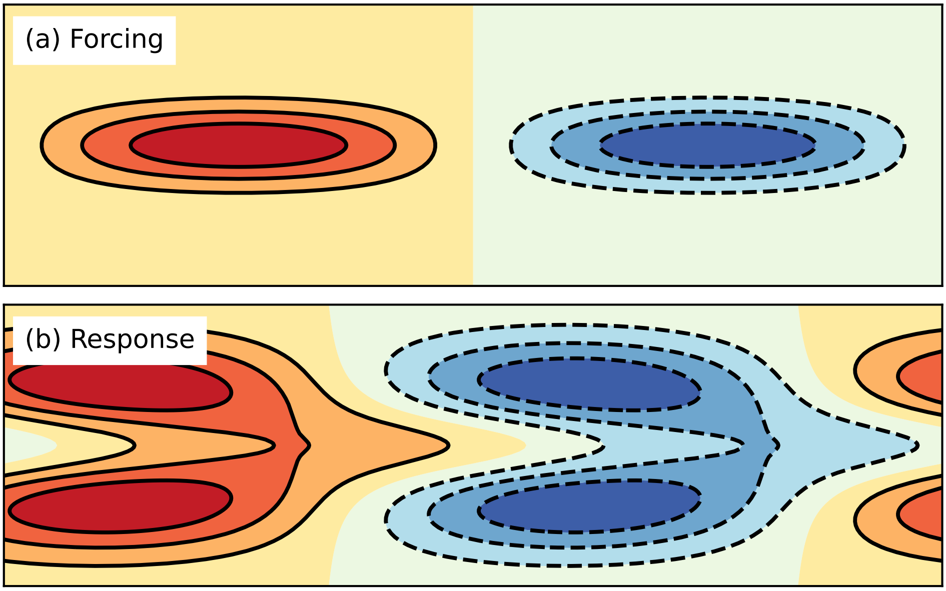

FIGURE 4. **La Fleur-de-lis on the sphere:** Height fields of the prescribed Kelvin wave 5 forcing (a) and the steady-state geopotential (b) for moderate damping and fast rotation (second row in figure 2). Color shading: numeric solutions obtained as detailed is section 4. Black contours: the β-plane approximation. Contours range from -1 to 1 every 0.25.

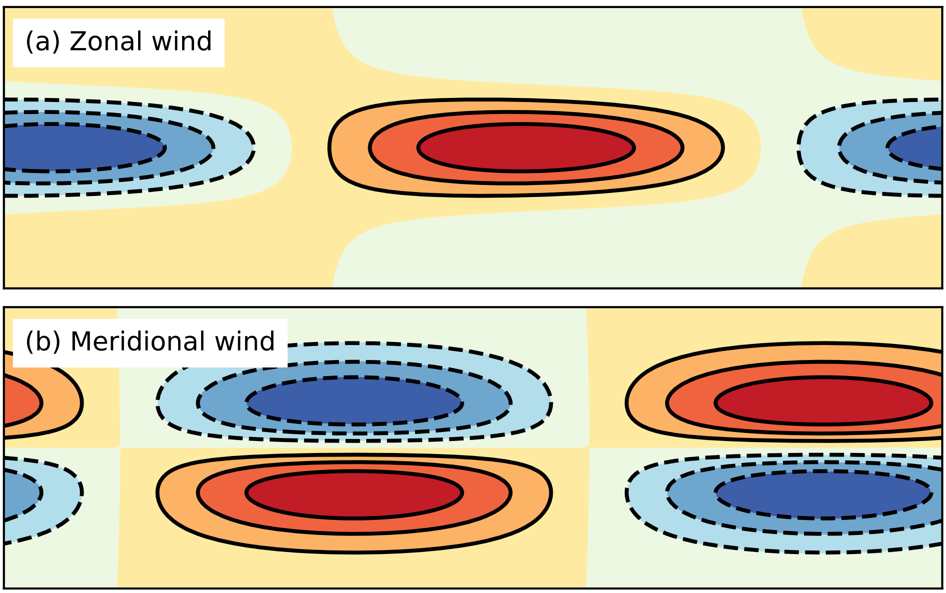

FIGURE 5. The steady-state zonal (a) and meridional (b) winds for moderate damping and fast rotation (second row in figure 2). Color shading: numeric solutions obtained as detailed is section 4. Black contours: the β-plane approximation. Contours range from -1 to 1 every 0.25.

plane, radiative relaxation, geostrophic, non-rotating, weak temperature gradient, and the longwave limits. Together, the regimes covered by these approximate solutions include most of the $(\gamma, \epsilon^{1/2})$ plane. We start with the β-plane approximation due to its correspondence with the original works of Matsuno and Gill. However, in terms of complexity, the simplest approximations are the radiative relaxation and geostrophic approximations, in which the unknowns u, v, Φ can be written in terms of the prescribed forcing Q using only simple algebraic operations. The β-plane and non-rotating approximations are more complex since the Matsuno-Gill model can only be reduced to a (different) boundary value problem with known solutions. The weak temperature gradient and longwave approximations provide no tangible simplification and are included for comparison.

To quantify the validity of each approximation, we use the following "metric" of relative difference:

$$\frac{\|X_r^m - X_a^m\|}{\|X_r^m\|} = \frac{\sqrt{(X_r^m - X_a^m, X_r^m - X_a^m)}}{\sqrt{(X_r^m, X_r^m)}}, \tag{5.1}$$

where $X^m = [u^m, v^m, \Phi^m]^T$ represent the solution vector of the Matsuno-Gill model (2.5), the subscript r denotes the reference solutions (the numeric solutions obtained as described in section 4), the subscript a denotes one of the approximate solutions derived below, and $(X, \bar{X})$ denotes the inner product:

$$(X, \bar{X}) = \int_{-\pi/2}^{\pi/2} X^T \bar{X} \cos\phi \, d\phi. \tag{5.2}$$

We choose the difference metric in (5.1) for two reasons. First, it assigns equal weights to all three unknowns, and hence provides an estimate of the approximation as a whole. Second, for the sake of uniformity with section 7, where we will use the inner product in (5.2) to find the projections of the Matsuno-Gill model solutions on the free wave solutions of the RSWEs. We find that a value of 0.1 is a convenient indicator of "visual" convergence in the sense that the solutions overlap and values lower than 0.1 lead to no visible improvements. For the sake of brevity, we refer to this metric simply as the "relative difference".

5.1. *The β-plane approximation*

As mentioned in section 2, for any fixed zonal wavenumber, the free RSWEs on the equatorial β-plane approximate the RSWEs on the sphere for large values of the Lamb number. We now show that this is also the case for the Matsuno-Gill model: the solutions obtained by Matsuno (1966) approximate the solutions on the sphere for sufficiently large values of ϵ. To this end we first re-scale system (2.3) to conform with Matsuno's scaling (Gill's scaling differs from Matsuno's by a factor of $\sqrt{2}$), where the horizontal length scale corresponds to the equatorial Rossby deformation radius, $(\sqrt{gH}/\beta)^{1/2}$ where $\beta = 2\Omega/a$, and the time scale corresponds to the Rossby deformation time, $(\sqrt{gH}\beta)^{-1/2}$. Under Matsuno's scaling, (2.3) becomes

$$-\epsilon^{1/4}\tilde{v}\sin\phi + \frac{\epsilon^{-1/4}}{\cos\phi}\frac{\partial\tilde{\Phi}}{\partial\lambda} = -\alpha\tilde{u} \tag{5.3a}$$

$$\epsilon^{1/4}\tilde{u}\sin\phi + \epsilon^{-1/4}\frac{\partial\tilde{\Phi}}{\partial\phi} = -\alpha\tilde{v} \tag{5.3b}$$

$$\frac{\epsilon^{-1/4}}{\cos\phi}\left[\frac{\partial\tilde{u}}{\partial\lambda} + \frac{\partial}{\partial\phi}(\tilde{v}\cos\phi)\right] = -\alpha\tilde{\Phi} + \tilde{Q}, \tag{5.3c}$$

where tildes are used to distinguished the quantities in Matsuno's scaling from their counterparts in (2.3), and α is used to denote the damping coefficient to match Matsuno's notation as well. The transformations between systems (2.3) and (2.1) is:

$$(\tilde{u}, \tilde{v}) = (u, v); \quad \tilde{\Phi} = \Phi; \quad \alpha = \epsilon^{-1/4}\gamma; \quad \tilde{Q} = \epsilon^{-1/4}Q. \tag{5.4}$$

As the horizontal wind components and the geopotential remain unchanged under the above transformation, we drop the tildes above those three variables. Note that Lamb number appears (with different powers) in front of the Coriolis term, the pressure gradient term, and the divergence terms in (5.3). It, therefore, has no unique interpretation under Matuno's scaling.

Next, in order to obtain the β-plane approximation, we must also change to local Cartesian coordinates. Using the equatorial Rossby deformation radius as the horizontal length scale, the longitude and latitude transformations are $(\lambda, \phi) = \epsilon^{-1/4}(x, y)$. Recall that system (2.3) was further simplified by considering its Fourier decomposition in λ. The corresponding transformation of the zonal wavenumber is $m = \epsilon^{1/4}k$, where k is the planner wavenumber. Upon introducing the Fourier decomposition, system (5.3) becomes

$$-\epsilon^{1/4}v^k \sin(\epsilon^{-1/4}y) + \frac{ik}{\cos(\epsilon^{-1/4}y)}\Phi^k = -\alpha u^k \tag{5.5a}$$

$$\epsilon^{1/4}u^k \sin(\epsilon^{-1/4}y) + \frac{d\Phi^k}{dy} = -\alpha v^k \tag{5.5b}$$

$$\frac{1}{\cos(\epsilon^{-1/4}y)}\left[iku^k + \frac{d}{dy}(v^k \cos(\epsilon^{-1/4}y))\right] = -\alpha\Phi^k + \tilde{Q}^k. \tag{5.5c}$$

Assuming u^k, v^k, Φ^k and $\tilde{Q}^k$ can all be expanded in power series of $\epsilon^{-1/4}$, expanding also the trigonometric functions in Taylor series in $\epsilon^{-1/4}y$, and retaining only zero-order terms yields

$$-v^k y + ik\Phi^k = -\alpha u^k \tag{5.6a}$$

$$u^k y + \frac{d\Phi^k}{dy} = -\alpha v^k \tag{5.6b}$$

$$iku^k + \frac{dv^k}{dy} = -\alpha\Phi^k + \tilde{Q}^k, \tag{5.6c}$$

which is identical to system (30) of Matsuno (1966) with $F_x = F_y \equiv 0$.

Matsuno outlines a general procedure for obtaining the solutions for arbitrary values of n, k, and α by expanding both the solution and forcing in series of the free wave solutions (the eigenfunctions of the free RSWEs on the equatorial β-plane). This procedure is symbolically convenient, but is less convenient when writing the analytic solutions explicitly. At least one reason is the fact that Matsuno's expressions involve the free wave frequencies, which are given by a cubic equation. A more convenient way for deriving the (exact) solutions of equation (5.6), which was taken by Gill, is to expand the solutions and forcing in series of Hermite functions, which are the eigenfunctions of the sub-space spanned by the meridional velocity. In addition, Matsuno carries out the analysis only for $n = 0$, $k = 0.5$, and $\alpha = 0.2$. Thus, for the sake of completeness, we re-derive the solutions below for arbitrary values of n, k, and α. To this end we first re-write system (5.6) as a single equation in v^k. Using the first row in (5.6) to eliminate u^k from the second and third rows yields

$$\frac{d}{dy}\begin{bmatrix} v^k \\ \Phi^k \end{bmatrix} = -\frac{1}{\alpha}\begin{bmatrix} iky & \alpha^2+k^2 \\ \alpha^2+y^2 & -iky \end{bmatrix}\begin{bmatrix} v^k \\ \Phi^k \end{bmatrix} + \begin{bmatrix} \tilde{Q}^k \\ 0 \end{bmatrix}. \tag{5.7}$$

Differentiating the first row with respect to y and using the first and second rows to eliminate Φ^k and $d\Phi^k/dy$, respectively, yields

$$\frac{d^2 v^k}{dy^2} - \left[\alpha^2 + k^2 + y^2 - ik\alpha^{-1}\right] v^k = \frac{d\tilde{Q}^k}{dy} - iky\alpha^{-1}\tilde{Q}^k. \tag{5.8}$$

Equation (5.8) can be solved by expanding both v^k and $\tilde{Q}^k$ in series of Hermite functions, i.e.

$$v^k(y) = \sum_{n=0}^{\infty} v_n^k \Psi_n(y) = \sum_{n=0}^{\infty} v_n^k H_n(y)\exp(-\frac{1}{2}y^2), \tag{5.9}$$

where v_n^k are the expansion coefficients, $H_n(y)$ are the (non-normalized) Hermite polynomials of degree n, and $\Psi_n(y)$ are the Hermite functions (i.e. the Hermite polynomials multiplied by a Gaussian envelope). The latter satisfy the following recurrence relations

$$x\Psi_n(x) = +\frac{1}{2}\Psi_{n+1}(x) + n\Psi_{n-1}(x) \tag{5.10a}$$

$$\frac{d\Psi_n(x)}{dx} = -\frac{1}{2}\Psi_{n+1}(x) + n\Psi_{n-1}(x), \tag{5.10b}$$

and the differential equation

$$\frac{d^2\Psi_n(x)}{dx^2} + (2n+1-y^2)\Psi_n(x) = 0. \tag{5.11}$$

In general, $\tilde{Q}^k$ is expanded similarly to v^k in (5.9). Fortunately, for large ϵ, the geopotential height of the Kelvin and MRG waves, used here as the prescribed forcing, is proportional to a single Hermite function,

$$\tilde{Q}^k(y) = Q_0\Psi_N(y) := Q_0 H_N(y)\exp(-\frac{1}{2}y^2), \tag{5.12}$$

where Q_0 is a constant amplitude, and $N = 0, 1$ for Kelvin, MRG waves respectively. The convergence of the wave forcing of the present work to the above expression was confirmed in Fig. 4(a) for a Kelvin wave-5 forcing at $\epsilon^{1/2} = 10^2$, and is also confirmed below for an MRG wave-5 forcing.

Substituting (5.9) and (5.12) in equation (5.8), and using the recurrence relations (5.10a) and differential equation (5.11), yields

$$\sum_{n=0}^{\infty} -[2n+1+\alpha^2+k^2-ik\alpha^{-1}]v_n^k\Psi_n = Q_0[-\frac{1}{2}(1+ik\alpha^{-1})\Psi_{N+1} + N(1-ik\alpha^{-1})\Psi_{N-1}]. \tag{5.13}$$

Equating the coefficients of Ψ_n, the solution is

$$v^k(y) = v_{N+1}\Psi_{N+1} + v_{N-1}\Psi_{N-1}, \tag{5.14}$$

where

$$v_{N+1} = \frac{1}{2}Q_0\frac{1+ik\alpha^{-1}}{2N+3+k^2+\alpha^2-ik\alpha^{-1}}, \tag{5.15a}$$

$$v_{N-1} = -NQ_0\frac{1-ik\alpha^{-1}}{2N-1+k^2+\alpha^2-ik\alpha^{-1}}. \tag{5.15b}$$

Using the first row of (5.7), the solution for Φ^k is

$$\Phi^k = \frac{1}{2}R_- v_{N+1}\Psi_{N+2} + \left[-(N+1)R_+ v_{N+1} + R_0 Q_0 + \frac{1}{2}R_- v_{N-1}\right]\Psi_N - (N-1)R_+ v_{N-1}\Psi_{N-2}, \tag{5.16}$$

for $N = 0, 1, 2, \ldots$, where $\Psi_{-2} \equiv 0$ and

$$R_0 = \frac{\alpha}{\alpha^2 + k^2}, \quad R_\pm = \frac{\alpha \pm ik}{\alpha^2 + k^2}. \tag{5.17}$$

Recall that α is real, so the denominators in the above expressions do not vanish. Finally, using the first row of (5.6), the solution for u^k is

$$u^k = \frac{1}{2}R_- v_{N+1}\Psi_{N+2} + \left[(N+1)R_+ v_{N+1} - \frac{ik}{\alpha}R_0 Q_0 + \frac{1}{2}R_- v_{N-1}\right]\Psi_N + (N-1)R_+ v_{N-1}\Psi_{N-2}. \tag{5.18}$$

Substituting (5.14), (5.18) and (5.16) into (5.6) confirms that they are indeed the sought solutions for any values of n, k, and α.

The convergence of the Matsuno-Gill model on the sphere to the Matsuno-Gill model on the β-plane was shown in figures 4 and 5, for $\epsilon^{1/2} = 10^2$, $n = 0$, $m = 5$ ($k = 0.5$), and $\gamma = 1$ ($\alpha = 0.1$, not 0.2 as in Matsuno). We can now quantify the convergence in the rest of the $(\gamma, \epsilon^{1/2})$ plane. Figure 6 shows the relative differences between the analytic approximations in (5.14), (5.16), and (5.18), and the numeric solutions as a function of γ and $\epsilon^{1/2}$. The differences were calculated as in (5.1) and are shown in logarithmic scale. For the sake of comparison with the other approximations obtained in section 5, the error scales in all sub-sections are identical (hence the colors in this figure are under-saturated). For example, the (-1) contour, corresponding to a value of 0.1, is emphasized in the figure by the white dashed lines. It can be seen that the β-plane approximation improves gradually with increasing $\epsilon^{1/2}$ and becomes accurate for Fast rotation rates. As we have seen in section 4, these cases correspond to the equatorial solution-regime. Hence, generally speaking (and unsurprisingly), the equatorial β-plane approximation is valid for the equatorial solution-regime.

The β-plane approximation for moderate damping and fast-to-slow rotation is shown in figure 7 (black contours), compared to the numeric solutions of the Matsuno-Gill model (shadings). The comparison is shown for the MRG wave-5 response: the black contours in the leftmost column correspond to the forcing in (5.12), confirming that the geopotential height of the MRG wave-5 under fast rotation can be approximated by a single Hermite function (the same was confirmed for the Kelvin wave-5 forcing in figure 4(a) and is also true for wave-1 forcing). The approximation breaks down, however, for moderate or slow rotation, as expected (figure 7 middle and bottom).

5.2. *The radiative relaxation approximation*

In section 4 we observed that for heavy damping, the forcing in the continuity equation is nearly balanced by the dissipation term, with only a negligible contribution of the divergence. For $\gamma \neq 0$, we can re-write the forcing as $Q = \gamma\tilde{\Phi}$, in which case the combination of the dissipation and forcing terms on the RHS of the continuity equation plays the role of a relaxation term $-\gamma(\Phi - \tilde{\Phi})$, with a relaxation time of $1/\gamma$. Hence this limit, and the ensuing approximation, can be thought of as a case where the geopotential height is relaxed towards the applied forcing. This is in contrast to light damping, where the forcing in the continuity equation is nearly balanced by the divergence term and the geopotential height is far from the applied forcing. We proceed by setting the dissipation term in the continuity equation (2.5*c*) equal to the forcing. The resulting approximation

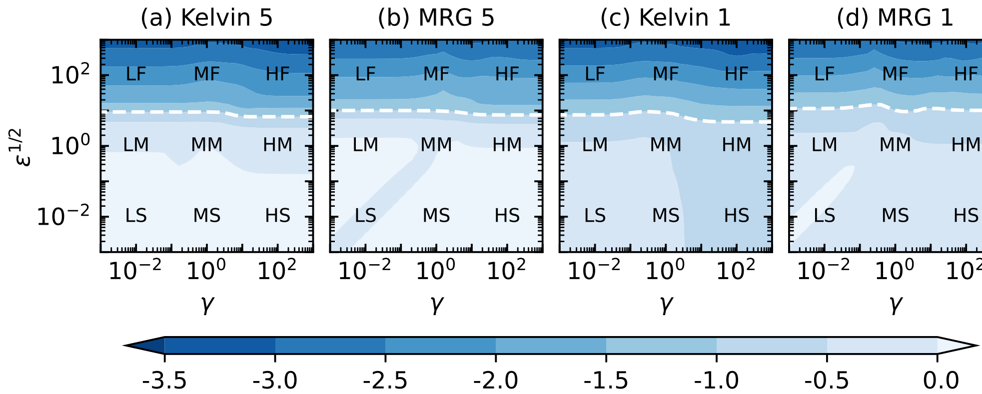

FIGURE 6. The relative difference (defined in (5.1)) between the β-**plane approximation** in (5.14), (5.16), and (5.18), and the numeric solutions obtained as described in section 4. The differences are shown in logarithmic scale. For example, the -1 contour, corresponding to a value of 0.1, is emphasized in the figure by the white dashed lines. For the sake of comparison with the other approximations obtained in section 5, the error scales in all sub-sections are identical. The particular samples of the $(\gamma, \epsilon^{1/2})$ plane defined in table 1 are also marked on the figure.

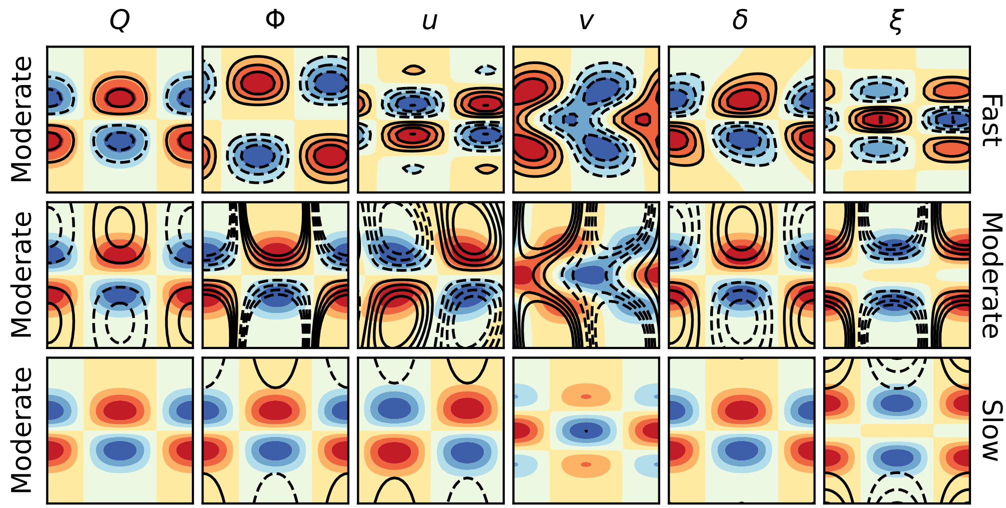

FIGURE 7. The β-**plane approximation** in (5.14)–(5.18) (black contours) superimposed on the steady response to an **MRG wave-5** forcing (shadings). The comparison is shown for a subset of figure 3 including moderate damping and fast rotation (MF), moderate damping and moderate rotation (MM), and moderate damping and slow rotation (MS). For the sake of clarity, the meridional domain of the equatorial regime in the first row zooms in on $[-20^\circ, 20^\circ]$.

for the geopotential height is

$$\Phi = \gamma^{-1} Q. \tag{5.19}$$

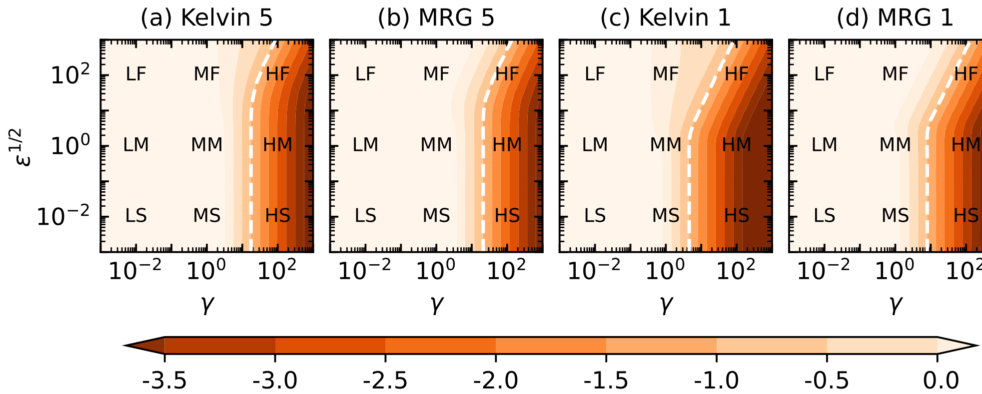

FIGURE 8. The relative difference (defined in (5.1)) between the **radiative approximation** in (5.19) and (5.21), and the numeric solutions obtained as described in section 4. The differences are shown in logarithmic scale. For example, the -1 contour, corresponding to a value of 0.1, is emphasized in the figure by the white dashed lines. For the sake of comparison with the other approximations obtained in section 5, the error scales in all sub-sections are identical. The particular samples of the $(\gamma, \epsilon^{1/2})$ plane defined in table 1 are also marked on the figure.

Substituting (5.19) into (2.5*a*) and (2.5*b*) yields the following second-order algebraic system for the horizontal velocity components

$$\begin{bmatrix} \gamma & -\epsilon^{1/2}\sin\phi \\ \epsilon^{1/2}\sin\phi & \gamma \end{bmatrix} \begin{bmatrix} u^m \\ v^m \end{bmatrix} = -\frac{1}{\gamma}\begin{bmatrix} \dfrac{im}{\cos\phi}Q^m \\ \dfrac{dQ^m}{d\phi} \end{bmatrix}. \tag{5.20}$$

For real $(\gamma, \epsilon) \neq 0$, this system has non-vanishing determinant so its unique solution is

$$u^m = -\frac{1}{\gamma^2 + \epsilon\sin^2\phi}\left[\frac{im}{\cos\phi}Q^m + \frac{\epsilon^{1/2}}{\gamma}\sin\phi\frac{dQ^m}{d\phi}\right], \tag{5.21a}$$

$$v^m = \frac{1}{\gamma^2 + \epsilon\sin^2\phi}\left[\frac{im\epsilon^{1/2}}{\gamma}\tan\phi Q^m - \frac{dQ^m}{d\phi}\right]. \tag{5.21b}$$

Figure 8 shows the relative difference between the radiative relaxation approximation in (5.19 and 5.21), and the numeric solutions as a function of γ and $\epsilon^{1/2}$. Indeed, the radiative relaxation approximation converges to the solutions of the Matsuno-Gill model on the sphere for heavy damping (albeit less so with fast rotation). The radiative relaxation approximation for the MRG wave-5 response with light-to-heavy damping and moderate rotation is shown in figure 9 (black contours), compared to the numeric solutions of the Matsuno-Gill model (shadings). As expected, the approximate solution and the exact solution match for heavy damping and are similar even for moderate damping, but diverge for light damping.

5.3. *The geostrophic approximation*

In section 4 we observed that the solutions of the Matsuno-Gill model with light damping and fast-to-moderate rotation rates are in geostrophic balance. We use this result to obtain additional simple solutions of the Matsuno-Gill model on the sphere. To this end, we set $\gamma = 0$ in (2.5), which yields a balance between the Coriolis and pressure gradient terms in the momentum equations and between the divergence and applied

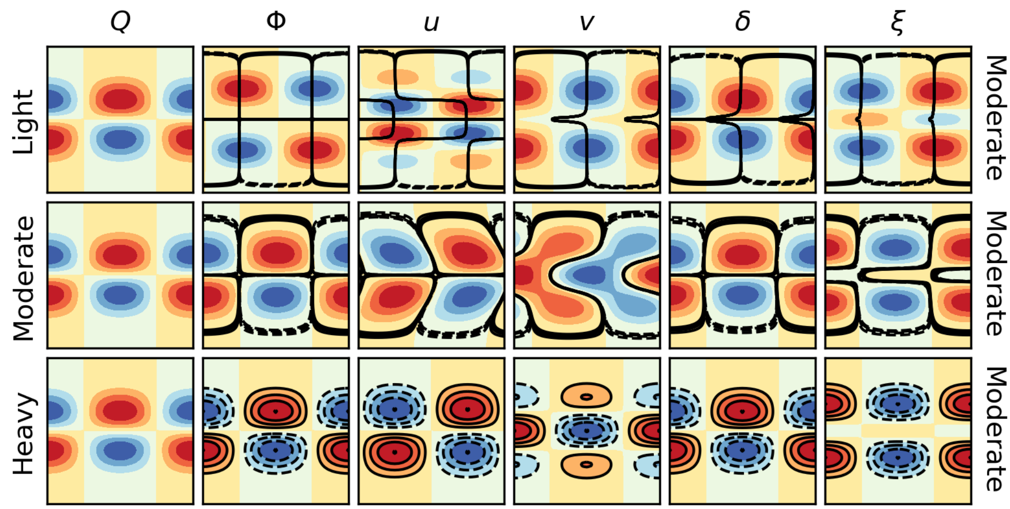

FIGURE 9. The **radiative relaxation approximation** in (5.19)–(5.21) (black contours) superimposed on the steady response to an **MRG wave-5** forcing (shadings). The comparison is shown for a subset of figure 3 including light damping and moderate rotation (LM), moderate damping and moderate rotation (MM), and heavy damping and moderate rotation (HM).

forcing in the continuity equation. The resulting equations correspond to the zero-order approximation of the Matsuno-Gill model in powers of γ and are given by

$$-\epsilon^{1/2} v^m \sin\phi + \frac{im}{\cos\phi}\Phi^m = 0 \tag{5.22a}$$

$$\epsilon^{1/2} u^m \sin\phi + \frac{d\Phi^m}{d\phi} = 0 \tag{5.22b}$$

$$\frac{1}{\cos\phi}\left[imu^m + \frac{d}{d\phi}(v^m\cos\phi)\right] = Q^m. \tag{5.22c}$$

Using (5.22b) and (5.22a) to substitute u^m and v^m in (5.22c), the derivative terms containing $d\Phi^m/d\phi$ cancel out leaving the following algebraic relation between the geopotential and the prescribed forcing

$$\Phi^m = \epsilon^{1/2}\frac{i}{m}\sin^2\phi\, Q^m. \tag{5.23}$$

Substituting (5.23) back into (5.22b) and (5.22a) yields the corresponding horizontal velocity components

$$u^m = -2\frac{i}{m}\cos\phi\, Q^m - \frac{i}{m}\sin\phi\,\frac{dQ^m}{d\phi}, \tag{5.24}$$

and

$$v^m = -\tan\phi\, Q^m. \tag{5.25}$$

Figure 10 shows the relative difference between the geostrophic approximation in (5.23)– (5.25), and the numeric solutions as a function of γ and $\epsilon^{1/2}$. Indeed, the geostrophic approximation converges to the solutions of the Matsuno-Gill model on the sphere for light damping and moderate-to-fast rotation (LM and LF). The geostrophic approximation of the MRG wave-5 response in these two cases, as well as for light damping and slow rotation (LS), is shown in figure 11 (black contours), compared to the numeric solutions of the Matsuno-Gill model (shadings).

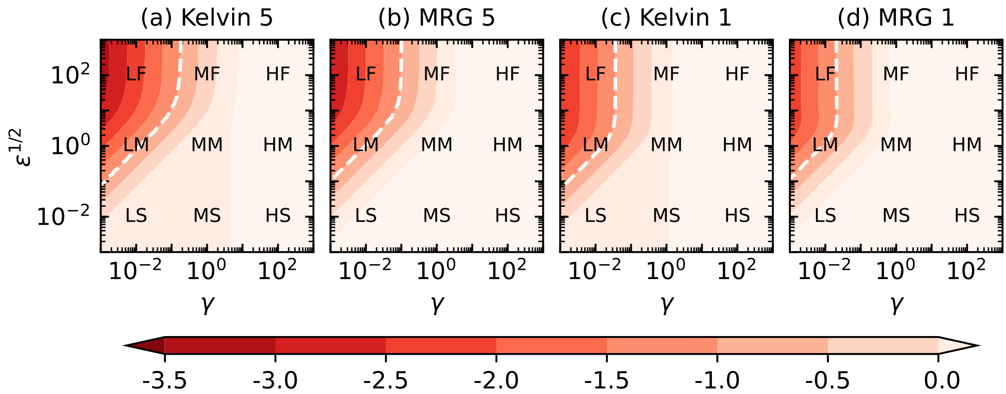

FIGURE 10. The relative difference defined in (5.1) between the **geostrophic approximation** in (5.23)–(5.25), and the numeric solutions obtained as described in section 4. The differences are shown in logarithmic scale. For example, the -1 contour, corresponding to a value of 0.1, is emphasized in the figure by the white dashed lines. For the sake of comparison with the other approximations obtained in section 5, the error scales in all sub-sections are identical. The particular samples of the $(\gamma, \epsilon^{1/2})$ plane defined in table 1 are also marked on the figure.

The geostrophic approximation in (5.23)–(5.25) corresponds to the zero-order approximation of the Matsuno-Gill model on the sphere in powers of γ. Adding the first-order terms yields only marginal improvements. The reason is that the solutions outside the LM and LF regions where the zero-order approximation is already fairly accurate, are highly a-geostrophic and the series solutions converge very slowly.

5.4. *The non-rotating approximation*

The non-rotating approximation reduces the order of the RSWEs from third-order to second-order in time (i.e. no Rossby waves) by setting the non-dimensional rate of rotation equal to zero, yielding the canonical wave equation. Similarly, setting $\epsilon^{1/2} = 0$ in the Matsuno-Gill model (2.5) yields

$$\frac{im}{\cos\phi}\varPhi^m = -\gamma u^m \tag{5.26a}$$

$$\frac{d\varPhi^m}{d\phi} = -\gamma v^m \tag{5.26b}$$

$$\frac{1}{\cos\phi}\left[imu^m + \frac{d}{d\phi}(v^m\cos\phi)\right] = -\gamma\varPhi^m + Q^m. \tag{5.26c}$$

Using (5.26b) and (5.26a) to substitute u^m and v^m in (5.26c) yields the following boundary value problem for the geopotential in terms of the specified forcing

$$\varDelta^m\varPhi^m = \gamma^2\varPhi^m - \gamma Q^m, \tag{5.27}$$

where $\varDelta^m$ is the m-restricted Laplacian operator defined as

$$\varDelta^m = \frac{1}{\cos\phi}\left[\frac{d}{d\phi}\left(\cos\phi\frac{d}{d\phi}\right) - \frac{m^2}{\cos\phi}\right]. \tag{5.28}$$

Equation (5.27) can be solved by expanding both $\varPhi^m$ and Q^m in series of Associated Legendre Polynomials (ALPs), which are the eigenfunctions of the m-restricted Laplacian

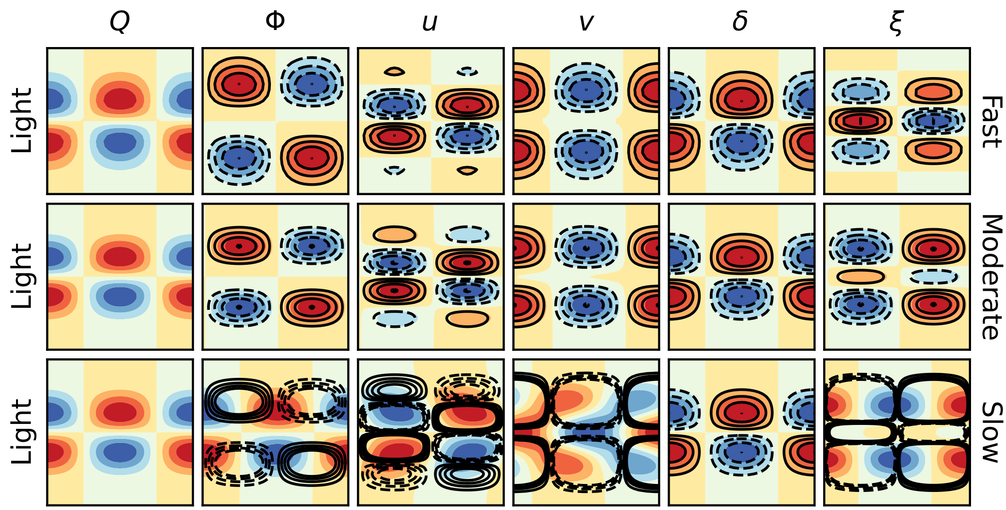

FIGURE 11. The **geostrophic approximation** in (5.23)–(5.25) (black contours) superimposed on the steady response to an **MRG wave-5** forcing (shadings). The comparison is shown for a subset of figure 3 including light damping and fast rotation (LF), light damping and moderate rotation (LM), and light damping and slow rotation (LS). For the sake of clarity, the meridional domain of the equatorial regime in the first row zooms in on $[-20°, 20°]$.

in (5.28). Specifically, let P_l^m denote the ALP of degree l and order m, then

$$\Delta^m P_l^m(\sin\phi) = -l(l+1)P_l^m(\sin\phi). \tag{5.29}$$

Fortunately, for $\epsilon^{1/2} \to 0$ the geopotential height field associated with the Kelvin and MRG waves can be accurately approximated by a single ALP. Thus, we proceed to find non-rotating solutions of the Matsuno-Gill model in response to the following prescribed forcing

$$Q^m(y) = Q_f^m P_l^m(\sin\phi), \tag{5.30}$$

where Q_f^m is a constant amplitude, and $l = m$ or $l = m+1$ for Kelvin or MRG waves, respectively. Substituting (5.30) into (5.27) and using (5.29), the solution for Φ^m in the non-rotating approximation is

$$\Phi^m = \frac{\gamma}{\gamma^2 + l(l+1)} Q_f^m P_l^m(\sin\phi). \tag{5.31}$$

Using (5.26*a*) and (5.26*b*), the corresponding solutions for u^m and v^m in the non-rotating approximation are

$$u^m = -\frac{im}{\gamma^2 + l(l+1)} \frac{Q_f^m}{\cos\phi} P_l^m(\sin\phi), \tag{5.32}$$

and

$$v^m = -\frac{1}{\gamma^2 + l(l+1)} Q_f^m \frac{dP_l^m(\sin\phi)}{d\phi}. \tag{5.33}$$

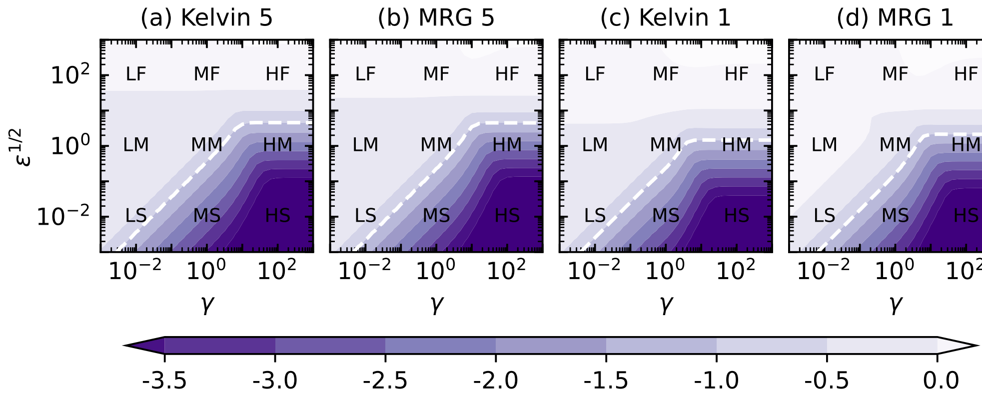

FIGURE 12. The relative difference defined in (5.1) between the **non-rotating approximation** in (5.31)–(5.33), and the numeric solutions obtained as described in section 4. The differences are shown in logarithmic scale. For example, the -1 contour, corresponding to a value of 0.1, is emphasized in the figure by the white dashed line. For the sake of comparison with the other approximations obtained in section 5, the error scales in all sub-sections are identical. The particular samples of the $(\gamma, \epsilon^{1/2})$ plane defined in table 1 are also marked on the figure.

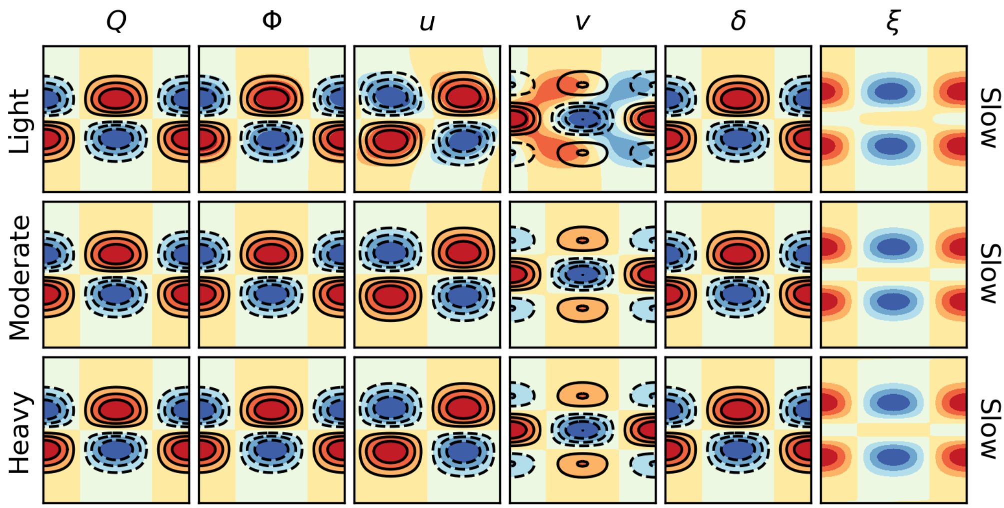

FIGURE 13. The **non-rotating approximation** in (5.31)–(5.33) (black contours) superimposed on the steady response to an **MRG wave-5** forcing (shadings). The comparison is shown for a subset of figure 3 including light damping and slow rotation (LS), moderate damping and slow rotation (MS), and heavy damping and slow rotation (HS).

Figure 12 shows the relative difference between the non-rotating approximation in (5.31)–(5.33), and the numeric solutions as a function of γ and $\epsilon^{1/2}$. As expected, the non-rotating approximation converges to the solutions of the Matsuno-Gill model on the sphere for moderate-to-heavy damping and slow rotation (MS and HS). In addition the non-rotating approximation can also approximate the solution for heavy damping and moderate rotation (HM). The non-rotating approximation for the MRG wave-5 response with slow rotation (and all damping rates) is shown in figure 13 (black contours), compared to the numeric solutions of the Matsuno-Gill model (shadings). Importantly, the black contours in the leftmost column correspond to forcing in (5.30), confirming the assumption that the geopotential height of the MRG wave can be approximated by a single ALP (the same is also true for the Kelvin wave). Finally, the vorticity in this approximation is identically zero, while the vorticity at moderate damping and slow rotation (MS) is far from small.

The non-rotating approximation in (5.31)–(5.33) corresponds to the zero-order approximation of the Matsuno-Gill model on the sphere in powers of $\epsilon^{1/2}$. Adding the first-order terms yields a more accurate approximation of the vorticity, but only marginal improvements in terms of the relative difference in (5.1). As we will see in section 7, the solutions outside the HM and HS regions are qualitatively different from non-rotating in terms of the excited waves.

5.5. *The weak temperature gradient approximation*

The accuracy of the geostrophic and non-rotating approximations is reduced at light damping and slow rotation. The reason is that, as established by Neelin (1988) and Bretherton & Sobel (2003), the Matsuno-Gill model becomes underdetermined when $\gamma = \epsilon^{1/2} = 0$. Specifically, the momentum equations mandate that $\Phi^m \equiv 0$ in that case, but the continuity equation only mandates that $\delta^m = Q^m$. Any combination of u^m and v^m that satisfies the last condition will therefore be a solution. As an alternative, Bretherton & Sobel (2003) studied the solutions obtained by setting the damping equal to zero only in the continuity equation, referred to as the weak temperature gradient (WTG) approximation. This idea is supported by our observations in section 4; as we have seen, with light damping, the forcing in the continuity equation is balanced by the divergence term, while the contribution of the dissipation term is negligible. Thus, we make the WTG approximation for the Matsuno-Gill model on the sphere by setting the damping equal to zero only in the continuity equation. This approximation yields no analytic simplification; we can only examine this approximation numerically.

Figure 14 shows the relative difference between the WTG approximation and full model solutions as a function of γ and $\epsilon^{1/2}$. Indeed, the WTG approximation matches the full model with light damping and slow rotation (LS), and is also “visually accurate” for light damping and fast rotation (LF), light damping and moderate rotation (LM), moderate damping and slow rotation (MS), and, most notably, moderate damping and moderate rotation (MM).

The WTG approximation for the MRG wave-5 response in the HF, MM, and LS cases is shown in figure 15 (black contours), compared to the numeric solutions of the Matsuno-Gill model (shadings). As observed in figures 2 and 3, the solutions for the LS and MM cases are similar, but not identical (in terms of the magnitudes of the fields). Finally, Bretherton & Sobel (2003) found that the Matsuno-Gill model under the WTG approximation has a far-field response, in the sense that the steady-state geopotential in response to an equatorially trapped forcing is not itself equatorially trapped. The situation for the Matsuno-Gill model on the sphere is somewhat different. With light damping and slow rotation, where the WTG approximation is most accurate,

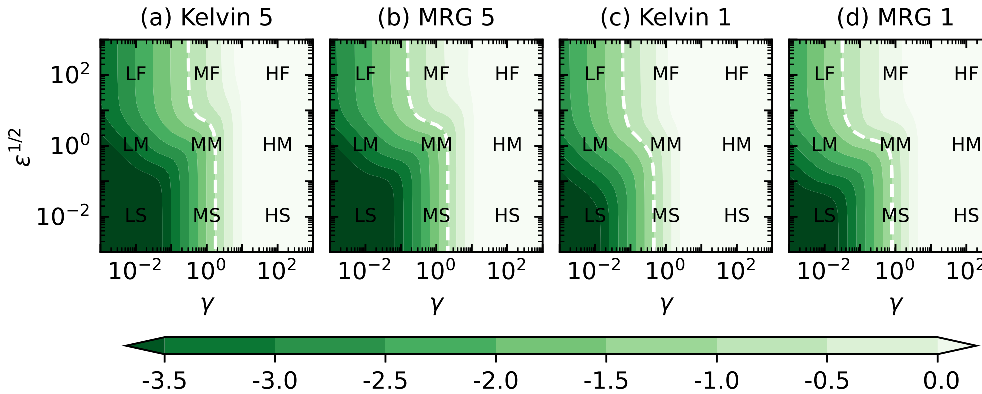

FIGURE 14. The relative difference (defined in (5.1)) between the **WTG approximation** and Matsuno-Gill model solutions obtained as described in section 4. The differences are shown in logarithmic scale. For example, the -1 contour, corresponding to a value of 0.1, is emphasized in the figure by the white dashed lines. For the sake of comparison with the other approximations obtained in section 5, the error scales in all sub-sections are identical. The particular samples of the $(\gamma, \epsilon^{1/2})$ plane defined in table 1 are also marked on the figure.

the extension of the forcing is no longer equatorially trapped. The WTG also provides an accurate approximation for light damping and fast rotation, where both the forcing and the response are equatorially trapped.

5.6. *The longwave approximation*

For the sake of completeness and comparison with Gill (1980), we now examine the longwave approximation obtained by setting the damping equal to zero only in the v-momentum equation. This approximation is not motivated by any of our observations in section 4. Yet, as we will see in section 6, it does improve on the geostrophic approximation for light damping and fast rotation, consistent with the fact that it is a less constrained version of the geostrophic approximation, where only the zonal wind is in geostrophic balance. Setting the damping equal to zero only in the v-momentum equation, one can derive a second-order boundary value problem in Φ^m. However, this boundary value problem has no simple solutions, so the longwave approximation does not provide simple solutions in the same sense the β-plane or non-rotating approximation do. Hence, we examine this approximation numerically.

Figure 16 shows the relative difference between the longwave approximation and Matsuno-Gill model solutions as a function of γ and $\epsilon^{1/2}$. The longwave approximation converges to the full model at light damping and fast rotation. It is also "visually accurate" for moderate damping and fast rotation, and to a lesser degree (only for the wave-5 response) for light damping and moderate rotation. The longwave approximation for the MRG wave-5 response in these three cases is shown in figure 17 (black contours), compared to the numeric solutions of the Matsuno-Gill model (shadings). Indeed, it is less accurate for light damping and moderate rotation, in the sense that Φ and u (and δ) are accurately approximated, but v (and ξ) are not.

6. Applicability to Earth, Venus, and Titan

We now consider our results in the context of the atmospheres and oceans of Earth and other planets, in particular with regard to the simple solutions obtained above. For

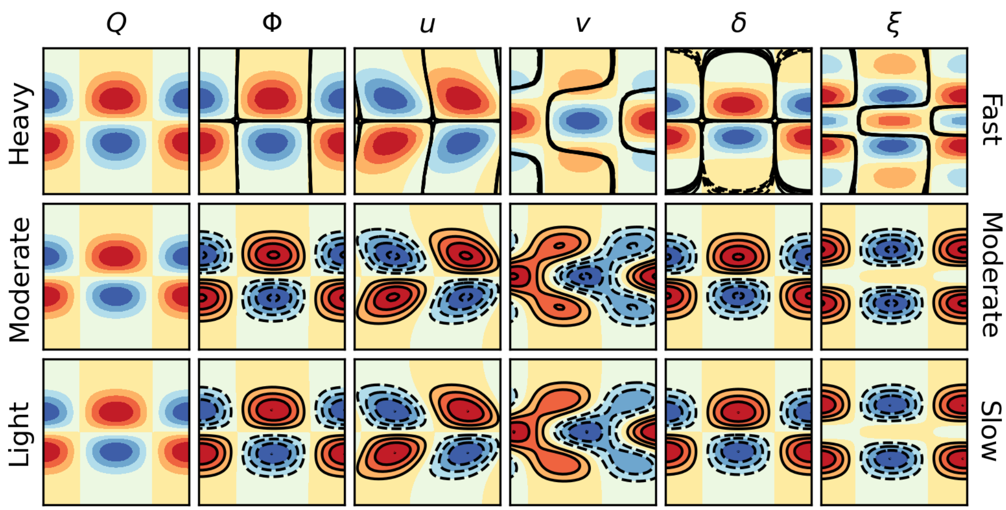

FIGURE 15. The **WTG approximation** (black contours) superimposed on the steady response to an **MRG wave-5** forcing (shadings). The comparison is shown for a subset of figure 3 including heavy damping and fast rotation (HF), moderate damping and moderate rotation (MM), and light damping and slow rotation (LS). For the sake of clarity, the meridional domain of the equatorial regime in the first row zooms in on $[-20°, 20°]$.

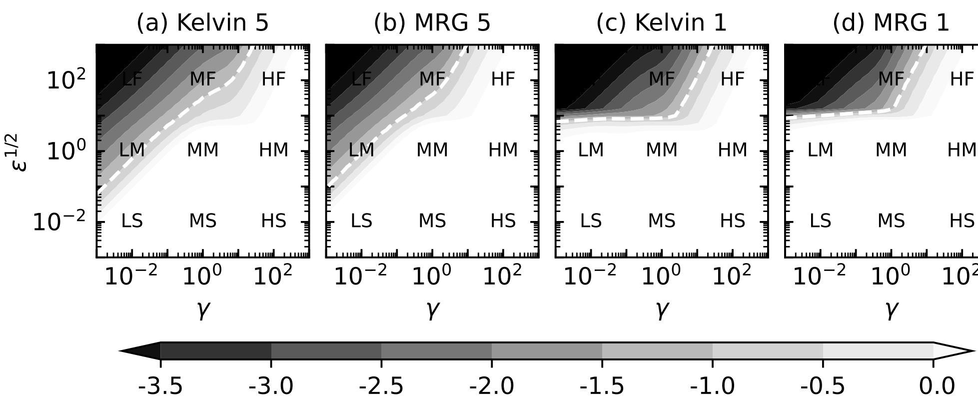

FIGURE 16. The relative difference (defined in (5.1)) between the **longwave approximation** and Matsuno-Gill model solutions obtained as described in section 4. The differences are shown in logarithmic scale. For example, the -1 contour, corresponding to a value of 0.1, is emphasized in the figure by the white dashed lines. For the sake of comparison with the other approximations obtained in section 5, the error scales in all sub-sections are identical. The particular samples of the $(\gamma, \epsilon^{1/2})$ plane defined in table 1 are also marked on the figure.

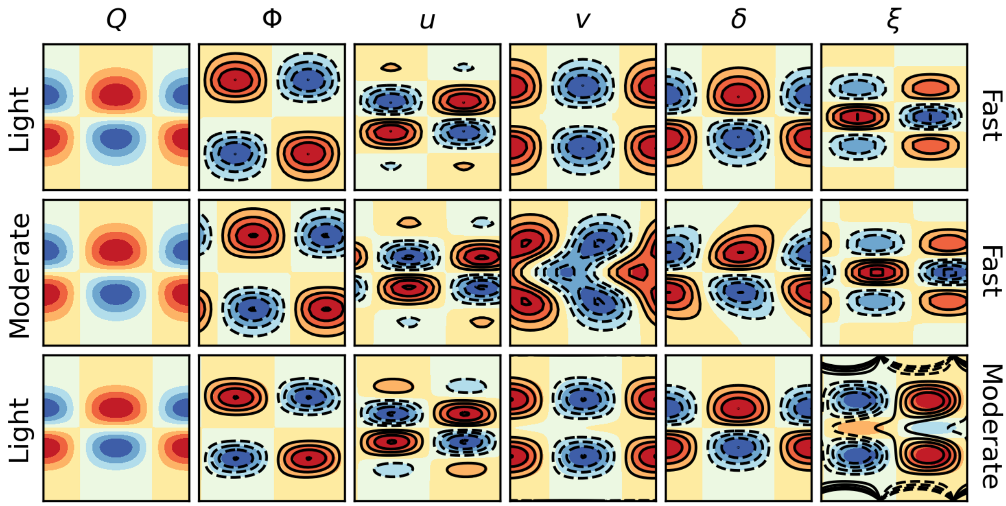

FIGURE 17. The **longwave approximation** (black contours) superimposed on the steady response to an **MRG wave-5** forcing (shadings). The comparison is shown for a subset of figure 3 including light damping and fast rotation (LF), moderate damping and fast rotation (MF), and light damping and moderate rotation (LM). For the sake of clarity, the meridional domain of the equatorial regime in the first two rows zooms in on $[-20°, 20°]$.

example, steady motion on Earth is generally believed to be near geostrophic balance, but, as we have seen in section 5.3, the steady solutions of the forced-dissipated RSWEs are only in geostrophic balance in a small subset of the $(\gamma, \epsilon^{1/2})$ plane. In general, the β-plane, radiative relaxation, geostrophic, and WTG approximations are all believed to be relevant to Earth, but each approximation accurately captures the solutions of the forced-dissipated RSWEs in different regions of the $(\gamma, \epsilon^{1/2})$ plane.

First, we establish where the different approximations are most relevant. Figure 18 combines the results of the subsections 5.1– 5.6: at each point of the $(\gamma, \epsilon^{1/2})$ plane we check for which of the six approximations the relative difference defined in (5.1) is smallest, and whether its values is smaller than or equal to 0.1. The latter condition is added to ensure that the best approximation is a good one. Clearly, the value of 0.1 is subjective; it is possible to extend the regions of validity of each approximation by considering a value of e.g. 0.2, but only to a small extent since the solutions soon become qualitatively different. The purpose of this figure is not to provide a quantitative comparison between the six approximations or locate the exact transitions between them, but rather to provide a qualitative overview. The geostrophic approximation was included in the comparison, but its accuracy is less than that of either the WTG or longwave approximation at every point in the $(\gamma, \epsilon^{1/2})$ plane.

The dashed rectangles in panels (a), (b), and (c) in figure 18 indicate the estimated regions of relevance to Earth's troposphere, stratosphere, and ocean, respectively. Using the mean radius, gravitational acceleration, and angular frequency of the Earth, the remaining unknown in Lamb number $\epsilon = (2\Omega a)^2/gH$ is the mean layer thickness H of the shallow water model. The rectangles shown in figure 18 correspond to values of H between the barotropic mode and first baroclinic mode in each case. The values of H in the atmosphere are based on the results of De-Leon *et al.* (2020), who estimated the "equivalent depth" for different background temperature profiles and boundary conditions. For the troposphere, we take H to be between 10 km and 100 m. For the stratosphere, we take H to be between 9 km and 3.5 km. For the ocean, we take H to be between 4 km and 0.5 m. The former is based on the mean ocean depth, and the latter on the estimations of Chelton *et al.* (1998). For the damping coefficient, we use values between 0.1 day^{-1} and 1 day^{-1}. Since the time scale introduced in section 2 involves H, the non-dimensional damping coefficient γ (the rectangles' width) in panels (a), (b), and (c) is different, even though the dimensional values are the same in all cases. Due to the logarithmic scale on both axes, slightly different estimations of the parameter lead to only small changes in the rectangle. Hence we argue that they are fairly representative of the troposphere, stratosphere, and oceans.

About half of the troposphere-relevant region is well approximated by the β-plane approximation, where it is also close to the region of the plane corresponding to the original results obtained by Matsuno and Gill (the MF region). On the other hand, about half of the troposphere relevant region is also qualitatively different from the β-plane approximation and is more accurately approximated by the WTG approximation. The stratosphere-relevant region is also qualitatively different from the β-plane approximation and is more accurately approximated by the WTG approximation. Finally, the ocean-relevant region is, for all practical matters, covered by the original results of Matsuno and Gill, with or without the longwave approximation.

In addition to our own planet Earth, the Matsuno-Gill model may also be of interest to Venus' and Titan's atmospheres, which are characterized by global-scale Hadley circulations and strong equatorial waves that flux westerly momentum towards the equator (Svedhem *et al.* 2007; Mitchell *et al.* 2011; Yamamoto 2019; Peralta *et al.* 2020). The dashed and solid rectangles in panel (d) of figure 18 indicate the estimated region of relevance to Venus' and Titan's tropospheres, respectively. For Venus, the range of ϵ used here is taken from Yamamoto (2019) to be $\epsilon^{1/2} = 11 - 160$, which in turn is based on different estimations of the speed of gravity waves in Venus' troposphere. For Titan, the upper limit of ϵ used here is taken from Yamamoto (2019) to be $\epsilon^{1/2} = 5.5$, corresponding to $H = 75$ m. For the lower limit we take a $H = 25$ km, corresponding to $\epsilon^{1/2} = 0.016$. This choice is based on the observation that the "equivalent depth" of the baroclinic mode tends to be of the same order of magnitude as the scale-height, which is between $H = 15-50$ km for Titan (Müller-Wodarg *et al.* 2014). For the damping coefficient we use values between 0.1-1 of the planet's period of rotation, as we did for Earth. Specifically, between $4.12 \cdot 10^{-4} - 4.12 \cdot 10^{-3}$ day^{-1} for Venus, and $6.25 \cdot 10^{-3} - 6.25 \cdot 10^{-2}$ day^{-1} for Titan.

The Venusian atmosphere is poorly characterized by most of these assumptions. Specifically, it falls within the region poorly described by all assumptions for wavenumber 1 for either the mixed Rossby-Gravity mode or the Kelvin mode. For higher wavenumbers the WTG approximation is somewhat better. However, the degree of success is sensitive to the precise value of damping used (which is poorly constrained by observations). The relative lack of success for Venus is consistent with observations showing a substantial meridional velocity for wavenumber 1 Kelvin waves in Venus' atmosphere (Belton *et al.* 1976; Covey & Schubert 1982; Del Genio & Rossow 1990; Smith *et al.* 1992; Yamamoto 2019; Peralta *et al.* 2020) that cannot be described by the Matsuno-Gill β-plane model of a fast rotating atmosphere.

Titan's atmosphere is well represented by the WTG approximation. The geostrophic

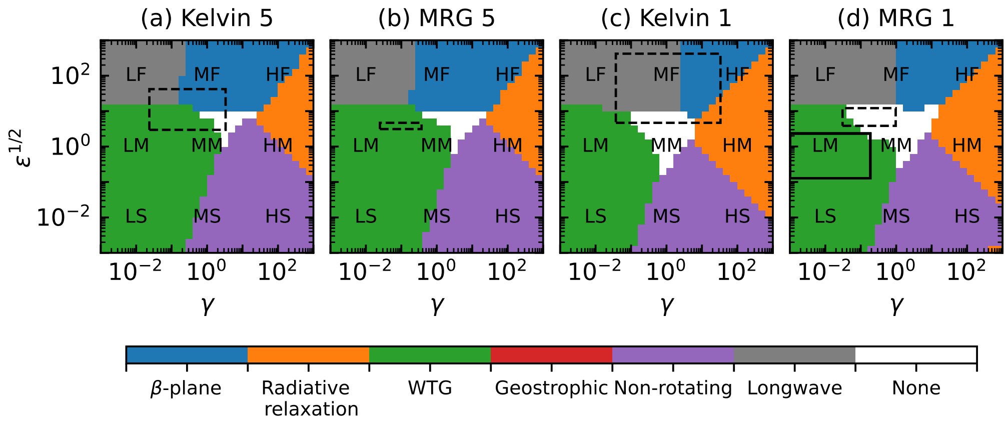

FIGURE 18. A comparison between the β-plane, radiative relaxation, geostrophic, and non-rotating approximations in terms. At each point of the $(\gamma, \epsilon^{1/2})$ plane the comparison is made by checking for which of the four approximations the relative difference defined in (5.1) is smallest, and whether its values is smaller than or equal to 0.1. The differences are shown in logarithmic scale. The particular samples of the $(\gamma, \epsilon^{1/2})$ plane defined in table 1 are also marked on the figure. Dashed rectangles on panels (a), (b), and (c) indicate the regions relevant to Earth's troposphere, stratosphere, and ocean, respectively, while the dashed and solid rectangles on panel (d) indicate the regions relevant to Venus' and Titan's tropospheres, respectively.

approximation also works in the region of relevance to Titan, and while it is less accurate than the WTG, it is analytic. A nonzero meridional component of an equatorial Kelvin(-like) wave is seen in a Titan General Circulation Model as well (Mitchell *et al.* 2011). This Kelvin wave part of the solution can be described by the ad-hoc solution of Garfinkel *et al.* (2017) which has a different functional form than the solutions of Longuet-Higgins (1968) and Matsuno (1966), however, this solution only applies to the Kelvin wave and not to other wave-modes.

7. Wave spectrum

A key feature of Gill's analysis is the description of the steady circulation in terms of the constituent waves. In the absence of analytic solutions of the Matsuno-Gill model on the sphere for arbitrary values of γ and ϵ, we proceed to find the constituent waves numerically by projecting the solutions on the spectrum of the free RSWEs. Let, $X_\omega = [u^m, v^m, \Phi^m]^T$ denote the eigen-solution of the free RSWEs corresponding to the eigenvalue (frequency) ω, obtained by solving (2.7) using the Chebyshev collocation method. Similarly, let $X_\gamma = [u^m, v^m, \Phi^m]^T$ denote the solution vector of the Matsuno-Gill model with a damping rate γ, obtained by solving (2.5) using the Chebyshev collocation method. The projection of the latter on the former is

$$\text{projection}_\omega = \frac{(X_\omega, X_\gamma)}{(X_\omega, X_\omega)}, \tag{7.1}$$

where $(X, \bar{X})$ is the inner product defined in (5.2). Note that the linear operator of the free RSWEs, $\mathcal{L}$ on the LHS of (2.7), is skew-Hermitian with respect to the inner product in (5.2), i.e. $(\mathcal{L}X, \bar{X}) = -(X, \mathcal{L}^* \bar{X})$, which guarantees that eigen-solutions corresponding to different frequencies are orthogonal. Having found the projections of X_γ on each of

(a) Kelvin wave-5 response

	EIG2	EIG1	EIG0	Kelvin	Rossby2	Rossby1	MRG	WIG1	WIG2	Sum
LF	-	44%	-	-	-	9%	-	47%	-	100%
MF	-	-	-	3%	-	97%	-	-	-	100%
HF	-	2%	-	50%	-	28%	-	20%	-	100%
LM	-	3%	-	3%	-	79%	-	5%	-	90%
MM	-	15%	-	2%	-	23%	-	43%	-	83%
HM	-	-	-	50%	-	-	-	49%	-	99%
LS	-	13%	-	10%	-	36%	-	11%	-	70%
MS	-	3%	-	3%	-	57%	-	29%	-	92%
HS	-	-	-	49%	-	-	-	50%	-	99%

(b) MRG wave-5 response

	EIG2	EIG1	EIG0	Kelvin	Rossby2	Rossby1	MRG	WIG1	WIG2	Sum
LF	30%	-	12%	-	5%	-	21%	-	32%	100%
MF	-	-	2%	-	93%	-	5%	-	-	100%
HF	2%	-	27%	-	27%	-	24%	-	20%	100%
LM	2%	-	1%	-	53%	-	32%	-	2%	90%
MM	14%	-	-	-	12%	-	23%	-	31%	80%
HM	1%	-	48%	-	-	-	-	-	49%	98%
LS	10%	-	11%	-	15%	-	24%	-	11%	71%
MS	3%	-	1%	-	40%	-	16%	-	29%	89%
HS	1%	-	48%	-	-	-	-	-	50%	99%

TABLE 2. Projections of the Matsuno-Gill model solutions on the free RSWEs wave modes. (a) In response to a Kelvin wave-5 forcing. (b) In response to an MRG wave-5 forcing. Reported values correspond to the percent fraction (accurate to 1%) of the total power projected on the (columns from left to right): EIG2, EIG1, EIG0, Kelvin, Rossby2, Rossby1, MRG, WIG1, and WIG2 wave modes. The classification of the modes follows the classification used in Matsuno (1966). The combined contribution of the eight modes is given in the last column from the left. The different rows correspond to the 9 samples of the $(\gamma, \epsilon^{1/2})$ plane given in Table 1. To improve the readability, 0% projections, to the retained accuracy, are replaced by dashes.

the resolved X_ω, we calculate the fractional spectral power associated with each one,

$$\text{power}_\omega = \frac{|\text{projection}_\omega|^2}{\sum_\omega |\text{projection}_\omega|^2}. \tag{7.2}$$

The resulting projections of the Kelvin wave-5 forcing on the free EIG2, EIG1, EIG0, Kelvin, Rossby2, Rossby1, MRG, WIG1, and WIG2 wave modes are given in Table 2(a). For the sake of comparison with the Matsuno-Gill model on the equatorial β-plane, we follow the classification of the free wave modes used by Matsuno. However, as noted by Garfinkel *et al.* (2017), from the point of view of the eigenvalue problem associated with the free RSWEs on the sphere, the Kelvin wave is more accurately classified as the lowest mode EIG wave.

Starting with the MF case (second row from the top), the response consists solely of the free Kelvin and Rossby1 waves, with the Kelvin wave contributing 3% of the total power and the Rossby1 wave contributing 97%. This result is consistent with the symmetric forcing case studied by Gill. However, the distribution between the two is different from that associated with Gill's solutions due to the different model setup (non-localized, periodic, forcing without imposing the long-wave approximation). The present model setup is more comparable to Matsuno's setup, and indeed, the unequal distribution between the Kelvin and Rossby1 waves is consistent with the fact that petals of the Fleur-de-lis in Matsuno's solution are more pronounced than its stem (Fig. 9 in Matsuno 1966, Fig. 1 of the present work).

Continuing with the equatorial solutions-regime, the LF and HF spectra are appreciably different from the MF spectrum in terms of the excited waves and their ratios, due to the different damping rates. The Kelvin wave forcing in the β-plane approximation is proportional to the lowest Hermite function $\Psi_0 = \exp(-y^2/2)$. Besides the Kelvin wave, Ψ_0 appears only in the geopotential height of the EIG1, Rossby1, and WIG1 waves. Hence only these four waves can be excited, and their ratios depend on the damping rate. Indeed, the contributions of these four waves in the equatorial solution-regime sum up to 100%. However, in contrast to the MF response, the LF response has no Kelvin wave contribution at all, and its main contributions come from the EIG1 (44%) and WIG1 (47%) waves, while the main contribution to the HF response is the Kelvin wave (50%), with substantial contributions from the Rossby1 (28%) and WIG1 (20%) waves.

The reason that the "Kelvin" and "MRG" wave forcing excite other waves beside the Kelvin and MRG waves themselves is that the forcing consists only of the geopotential part of those waves. A true Kelvin or MRG wave (or any other wave mode) forcing consists of the unique $X = [u^m, v^m, \Phi^m]^T$ triplet associated with that wave, and the response of the linear Matsuno-Gill model to such a forcing would consist solely of that wave as well.

Moving on to the global solution-regime, the HM and HS responses consist solely of the free Kelvin and WIG1 waves, with each contributing 50% (within the retained accuracy) of the total power. As observed in sections 4 and 5.2, the forcing in the HM and HS responses is nearly balanced by the dissipation term (i.e. $-\gamma\Phi$), with the contribution of the divergence in the continuity equation being negligible. In addition, as observed in section 5.4, these two cases are accurately approximated by the non-rotating approximation, which consists of identical pairs of oppositely propagating gravity waves (no Rossby and MRG waves). Thus, the time-independent forcing projects equally on the first eastward and westward gravity waves, manifested as the Kelvin and WIG1 waves in this limit. In contrast to the HM and HS responses, the main contributions to the MS response are the Rossby1 wave (57%) and WIG1 wave (29%), with the Kelvin and EIG1 waves contributing only little (3% each). However, the dissipation term in the continuity equation in that case is an order of magnitude smaller than the divergence term and the forcing projects on the Rossby1 wave as well.

The main contribution to the LM response is the Rossby1 wave (79%), with the Kelvin (3%), EIG1 (3%), and WIG1 (5%) waves contributing only little. As we have seen in section 5.3, this case is accurately approximated by the geostrophic approximation, explaining the preferential Rossby wave excitation. Typically, the IG and Kelvin waves, propagate away during geostrophic adjustment (the transient part of the solution), leaving only the Rossby waves in the long-term solution.

Our main observation regarding the MM and LS responses is the fact that the total power contained in the first nine wave modes reported in Table 2 account for only 83% and 70%, respectively. Examining the subsequent wave modes, we find that the EIG3 and WIG3 waves account for additional 7% of the total power in the MM response (bringing the contribution of the first 11 waves modes up to 90%), and 14% of the total power in LS responses (bringing the contribution of the first 11 waves modes up to 84%). In other words, the expansion of the response in terms of the free wave modes converges slower in these two cases compared to all other cases. This observation is likely a different manifestation of the difficulty associated with finding simple (analytic) approximations (excluding the WTG) in these two cases.

Finally, the resulting projections of the MRG wave-5 forcing on the free EIG2, EIG1, EIG0, Kelvin, Rossby2, Rossby1, MRG, WIG1, and WIG2 wave modes are given in Table 2(b). In general, the above discussion with appropriate substitutions describes this case as well. In particular, the MRG wave forcing in the β-plane approximation is proportional to the second lowest Hermite function $\Psi_1 = 2y\exp(-y^2/2)$. Besides the MRG wave, Ψ_1 appears only in the geopotential height of the EIG2, EIG0, Rossby2, and WIG2 waves. Hence only these five waves can be exited, and indeed their contributions in the equatorial solutions-regime sum up to 100%. The main contribution to the MF response is the Rossby2 wave (93%), with the EIG0 (2%) and MRG (5%) waves contributing only little. This result is inconsistent with the anti-symmetric forcing case studied by Gill, where the response to the MRG wave consists solely of the EIG0 and MRG waves. However, again, the present model setup is more comparable to Matsuno's setup.

The main difference between the Kelvin and MRG wave responses is in the symmetry of the spectrum. The free RSWEs have a definite meridional symmetry, such that consecutive wave modes have opposite symmetries (e.g. in terms of $\Phi^m(\phi)$). If the forcing has a definite symmetry, then the solutions of the Matsuno-Gill model would have a definite symmetry as well. Considering the forcing is applied via the continuity equation, it can only excite waves having the same symmetry in terms of $\Phi^m(\phi)$. In the nonlinear case, however, this is not true: a purely antisymmetric forcing preferentially excites symmetric modes due to triad interactions, as discussed in detail in Garfinkel *et al.* (2021), Shamir *et al.* (2021*b*), and Shamir *et al.* (2021*a*).

Aside from the exploration of the $(\gamma, \epsilon^{1/2})$ plane, the wave spectrum is the key distinction between the Matsuno-Gill model on equatorial β-plane and its counterpart on the sphere. The effect of the Lamb number is to alter the eigenmodes of the free RSWEs and, therefore, the waves that can be excited by a given forcing.

8. The response to a local forcing

As discussed in section 3, the forcing used by Matsuno and Gill corresponds to the geopotential height of the Kelvin and MRG waves. Hence a natural extension of forcing for the model on the sphere is the geopotential height corresponding to these two waves. A limitation of this choice, however, is the fact that the resulting forcing in the equatorial solutions-regime is equatorially trapped, while the resulting forcing in the global solutions-regime is global. One is often interested in the global response to a local forcing, which is the focus of this section. In addition to making the forcing meridionally localized, we also demonstrate the applicability of our results to a zonally localized forcing akin to that used by Gill (1980).

Specifically, we study the response to the following forcing

$$Q(\lambda,\phi)=\begin{cases}\cos(3\lambda)\exp[-(24\phi/\pi)^2/2], & \text{for } |\lambda|\leqslant\pi/6,\\ 0, & \text{for } |\lambda|>\pi/6.\end{cases} \tag{8.1}$$

As discussed in section 2, due to the linearity of the Matsuno-Gill model and the λ-independence of the coefficients, we may study each Fourier mode separately. The Fourier series of the above forcing can be obtained analytically as follows

$$Q(\lambda,\phi)=\sum_{m=-\infty}^{\infty} Q_0^m \exp(im\lambda)\exp[-(24\phi/\pi)^2/2], \tag{8.2}$$

where

$$Q_0^m=\begin{cases}\dfrac{1}{12}, & \text{for } m=\pm 3,\\ \dfrac{1}{2\pi}\left[\dfrac{\sin[(3+m)\frac{\pi}{6}]}{3+m}+\dfrac{\sin[(3-m)\frac{\pi}{6}]}{3-m}\right], & \text{otherwise.}\end{cases} \tag{8.3}$$

Thus, we solve (2.5) for each Fourier mode numerically as described in section 4, substituting $\exp[-(24\phi/\pi)^2/2]$ for Q^m, and then sum the solutions according to (8.2) and (8.3).

The results are presented in figure 19 for a truncation of wavenumbers 50, i.e., $m=-50,\ldots,50$. As noted by Bretherton & Sobel (2003), if the damping term in the continuity equation is zero, the Matsuno-Gill model does not admit a non-zero zonal mean. Thus to avoid complications when the damping term in the continuity is small, we remove the $m=0$ Fourier mode from the results in this figure. As in figure 2, the leftmost column corresponds to the applied forcing, which is identical in all cases in this figure. Unlike figure 2 (and all other previous figures), the longitudinal domain corresponds to $[-\pi,\pi]$ (and not 1 zonal period). The meridional domain still extends from the south pole to the north pole.

In the response to moderate damping and fast rotation (second row in figure 19), we identify Gill's version of the Fleur-de-lis in the geopotential height field (red square). In the response to light damping and fast rotation (first row), we identify the Sverdrup balance approximation shown in Bretherton & Sobel (2003) for the Matsuno-Gill model on the equatorial β-plane in the limit of no damping (also discussed in Neelin 1988).

The key observation from figure 19 relates to the far-field response. In the response to light damping and moderate rotation (fourth row), we identify the WTG approximation obtained in Bretherton & Sobel (2003) for the Matsuno-Gill model on the equatorial β-plane. While the solutions in this case resemble those of Bretherton & Sobel, they correspond to different regimes in terms of the Rossby deformation radius. In Bretherton & Sobel, the e-folding of the forcing is $\sqrt{2}R_{\text{eq}}$, where R_{eq} is the equatorial Rossby deformation radius, and the resulting geopotential under the WTG approximation decays over several R_{eq}. The equatorial Rossby radius of deformation in the scaling of the present work is $R_{\text{eq}}=(gHa^2/4\Omega^2)^{1/4}=a\epsilon^{-1/4}$. For moderate rotation, where $\epsilon^{1/2}=1$, $R_{\text{eq}}=a=6371$ km, or about 57° latitude. Thus, in contrast to the WTG on the equatorial β-plane, the e-folding of the forcing in (8.1) corresponds to about $0.13R_{\text{eq}}$, and the geopotential decays within one R_{eq}. Considering the wave spectra in table 2, we see that the cases exhibiting far-field response are also the ones whose response is dominated by the Rossby waves (except for the moderate damping and moderate rotation case).

The results of this section demonstrate the generality and applicability of the results of the previous sections to the case of localized forcing. This is particularly important for applications such as quasi-stationary Rossby waves forced by the MJO or El Niño, where the forcing is indeed localized.

9. Summary and Discussion

In its essence, the Matsuno-Gill model is a driven harmonic oscillator in the atmosphere and oceans. An external force (a heat source or topography) provides potential energy, some of which is transferred to kinetic energy, some is dissipated by a linear drag, and the long-term response consists solely of those eigenmodes (equatorial waves) which are closest to being in resonance with the forcing. It is this essence which makes the Matsuno-Gill model instrumental in the study of the atmosphere and oceans. Yet, in its original formulation, the model employs the β-plane approximation, which, depending on the celestial body in question and the external forcing, may limit its applicability to the equatorial region. In the present work, we have extended the Matsuno-Gill model to the sphere.

The key difference between the model on the β-plane and its counterpart on the sphere lies in their parameter space. When applied to the equator, the β-plane approximation greatly simplifies the analysis by coupling the planetary rate of rotation and mean radius, thereby reducing the parameter space. In fact, on the equatorial β-plane, the Matsuno-Gill model can be reduced to a 1-dimensional parameter space, consisting solely of the non-dimensional rate of damping (γ), whereas, on the sphere, it can only be reduced to a 2-dimensional parameter space $(\gamma, \epsilon^{1/2})$. Depending on the choice of scaling, the additional parameter may play the role of the non-dimensional rate of rotation (the present choice), the non-dimensional gravitational acceleration, or the non-dimensional speed of gravity waves. Regardless of its interpretation, its effect is to alter the eigenmodes of the free system (the "natural frequencies" of the harmonic oscillator). Thus, unlike the solutions obtained by Matsuno and Gill, where the long-term response to a symmetric forcing consists solely of Kelvin and Rossby waves, the response of the Matsuno-Gill model on the sphere consists of other waves as well, depending on γ and $\epsilon^{1/2}$.

By considering the different combinations of damping and rotation, relative to the timescale a gravity wave can propagate appreciably around the sphere, we are able to effectively span the $(\gamma, \epsilon^{1/2})$ plane. We find that the β-plane approximation is accurate only with fast rotation, $\epsilon^{1/2} \gg 1$, while the particular solution studied by Matsuno and Gill is only accurate in the case of moderate damping (i.e., waves are damped on the same timescale as they propagate). The remaining regions of the parameter space can be described by appropriately simplified approximations.

With moderate rotation, $\epsilon^{1/2} \approx 1$, the most appropriate approximation depends on the damping. With light damping, $\gamma \ll 1$, the weak temperature gradient approximation (WTG), where the forcing is balanced by the flow divergence, is the most accurate. Less accurate, but analytic, solutions can be obtained with the geostrophic approximation, where the Coriolis and pressure gradient forces are also in balance. With heavy damping, $\gamma \gg 1$, accurate solutions can be found with a radiative relaxation approximation, where the forcing is balanced by the thermal dissipation.

With slow rotation, $\epsilon^{1/2} \ll 1$, and light damping, $\gamma \ll 1$, the WTG approximation is, again, the most accurate. With stronger damping, $\gamma \approx 1$ or $\gamma \gg 1$, the solutions can be captured with the non-rotating approximation, where the Coriolis force is neglected. Finally, cases with moderate rotation and damping, $\epsilon^{1/2} \approx \gamma \approx 1$, are the most difficult, and do not fall into any simple limit. To some extent, however, they may be captured with the WTG approximation. Interestingly, the results of the present work suggest that,

FIGURE 19. Steady-state response to the local forcing in 8.1. In order from left to right: the prescribed forcing, the geopotential height, the zonal wind, the meridional wind, the divergence, and vorticity. The different rows correspond to the different samples of $(\gamma, \epsilon^{1/2})$ plane summarized in table 1. The damping and rotation rates for each case (row) are labeled on the left and right edges, respectively. The meridional domain in each panel extend from the south pole to the north pole. The longitudinal domain in panel corresponds $[-\pi, \pi]$. Contours range from -1 to 1 every 0.2, excluding 0. For the sake of presentation, each panel is normalized on its global absolute maximum, given in white text boxes.

in the context of the Matsuno-Gill model, the WTG approximation is more accurate on a global-scale.

In terms of application to real geophysical fluids, we estimate that the majority of the Earth's oceans fall within the region of the $(\gamma, \epsilon^{1/2})$ plane corresponding to moderate damping and fast rotation, where the particular solution obtained by Matsuno and Gill are applicable. Earth's troposphere falls between the regions of light-to-moderate damping and fast-to-moderate rotation, half of which can be described by the β-plane approximation (fast rotation), and the other half by the WTG approximation (for sufficiently high forcing wavenumber). Earth's stratosphere falls roughly between the regions of light-to-moderate damping and moderate rotation, which can be described by either the WTG approximation or the geostrophic approximation, but not the β-plane approximation. Likewise for Titan's troposphere, which falls near the region of light damping and moderate rotation. Finally, Venus' troposphere falls close to the moderate damping and moderate rotation region, where no approximation is satisfactory.

One caveat of the Matsuno-Gill model is the linearization. Both the present work and the original studies by Matsuno and Gill employ the linearized Rotating Shallow Water Equations (RSWEs). However, the assumptions that justify the linearization involve both the amplitude and spatial distribution of the forcing. For highly oscillatory forcing, even small amplitude perturbations can drive localized, non-negligible advection of momentum and/or mass. Moreover, the linearization is about a resting basic state with no mean flow. The results derived above will likely be altered significantly by addition of a mean flow, as such westerly flows which enable Rossby wave propagation in the midlatitudes (Hoskins & Karoly 1981) and act as a waveguide (Hoskins & Ambrizzi 1993). In particular, we expect a spherical model linearized about a basic state with nonzero zonal flow to exhibit a canonical poleward arching Rossby wavetrain. This wavetrain will reach latitudes in which the equatorial β-plane assumption is grossly violated, necessitating the spherical formulation.

In formulating the Matsuno-Gill model we have conceptualized the prescribed forcing as being due to time-independent external forces, e.g., topography or solar radiation. One can also consider the quasi-steady-state response to internal variability on larger time scales, e.g., the quasi-stationary Rossby wave response to convective forcing by the MJO or El Niño. The Matsuno-Gill model turns out to be a useful theoretical framework for understanding the subsequent responses even for such quasi-stationary heat sources (Ángel F. Adames & Wallace 2014; Zhang *et al.* 2020). The spherical solutions considered here, particularly those in section 8, coupled with a mean flow could allow further study of the remote response to the tropical convective forcing associated with the MJO and El Niño. Specifically, the subtropical highs forced by ENSO and the MJO can be accounted for, albeit in a conceptual sense, by the Matsuno-Gill model. The classical papers on how the midlatitude lows come about (e.g. Hoskins & Karoly 1981) assume or impose a given subtropical convergence anomaly as a starting point. To date, there is no single overarching theory that can account for both the near-field (i.e. within the tropics) and far-field (i.e. midlatitude) responses to the MJO or El Niño. Solutions of the Matsuno-Gill problem on the sphere linearized about an appropriate background wind, however, may be able to account for the entirety of the Rossby wavetrain forced from the Tropics.

Another caveat of the Matsuno-Gill model is the source of the linear damping. The physical justification for the use of linear damping in the atmosphere has been examined by several authors throughout the years. By analyzing the steady-state vorticity budget, Holton & Colton (1972) found it necessary to have ostensibly heavy damping in order to obtain comparable results to the observed 200 hPa vorticity field during June-August 1967. They conjectured that the required heavy damping effectively plays the role of upward eddy momentum flux associated with subgrid-scale convection. By comparing the same observational data with general circulation model simulations, Sardeshmukh & Held (1984), suggested that the required heavy damping can also be explained by the resolved advection. Lin *et al.* (2008) further examined the contributions of these two mechanisms to the effective linear damping in the context of the Walker circulation. By examining the linearized zonal momentum budget in reanalysis data, they found that the two mechanisms have different contributions in different regions of the circulation. Finally, Romps (2014) found that convective momentum transport can explain the heavy damping of the large-scale circulation depending on the vertical wavenumbers. Regardless of the particular mechanism, these authors agree that heavy linear damping acts as a surrogate for missing nonlinearities. In the spirit of the present work, one may conclude that, when it comes to La Fleur-de-lis, "Vive la résistance".

A more glaring/nuanced caveat relating to the linear damping in the Matsuno-Gill model, not considered by the above authors, is the use of identical rates of "mechanical" damping in the momentum equations and "thermal" damping in the continuity equation. The former can only remove energy, whereas the latter plays the role of both dissipation and relaxation and thus can also add energy. As a result, the rate of energy intake in the Matsuno-Gill model is identical to the rate of energy loss, which is an unlikely scenario, especially if the linear damping is to be considered as a surrogate for the missing nonlinearities. Future work should consider the Matsuno-Gill model in the presence of different mechanical and thermal damping rates (ideally, the continuity equation should include separate damping and relaxation terms), and the observational justification for doing so.

These caveats said, we have shown that extending the Matsuno-Gill model from the β-plane to the sphere opens up a much richer space of solutions and applications. Not only does it allow us to capture solutions that extend sufficiently poleward for spherical geometry to play a role, the addition of a second parameter to capture the relative effects of rotation and damping allows one to explore additional regimes outside the scope of the original model. As we have shown, the original model is only appropriate when the rotation is fast relative to the time scale waves can appreciably propagate about the sphere. This is the most appropriate regime for Earth's oceans, and to a lesser extent the tropical troposphere – Matsuno and Gill knew what they were doing – but other regimes, both on Earth (e.g., our stratosphere) and beyond (e.g., Venus and Titan) become accessible with a formulation on the sphere.

The Authors thank Dr. O. Adam from the HU for helpful discussion on the tropical dynamics. OS and EPG acknowledge support from Schmidt Futures, a philanthropic initiative founded by Eric and Wendy Schmidt, as part of the Virtual Earth System Research Institute (VESRI). EPG acknowledges further support from the National Science Foundation (NSF, grant OAC-2004572).

REFERENCES

Adam, Ori 2018 Zonally varying itcz s in a matsuno-gill-type model with an idealized bjerknes feedback. *Journal of Advances in Modeling Earth Systems* **10** (6), 1304–1318.

Adames, Ángel F & Kim, Daehyun 2016 The mjo as a dispersive, convectively coupled moisture wave: Theory and observations. *Journal of the Atmospheric Sciences* **73** (3), 913–941.

Arnold, Nathan P, Tziperman, Eli & Farrell, Brian 2012 Abrupt transition to strong superrotation driven by equatorial wave resonance in an idealized gcm. *Journal of the Atmospheric Sciences* **69** (2), 626–640.

Belton, Michael JS, Smith, Gerald R, Schubert, Gerald & Del Genio, Anthony D 1976 Cloud patterns, waves and convection in the venus atmosphere. *Journal of Atmospheric Sciences* **33** (8), 1394–1417.

Biello, Joseph A & Majda, Andrew J 2005 A new multiscale model for the madden–julian oscillation. *Journal of the atmospheric sciences* **62** (6), 1694–1721.

Boyd, John P 2018 *Dynamics of the Equatorial Ocean*. Springer.

Boyd, John P & Zhou, Cheng 2008 Uniform asymptotics for the linear kelvin wave in spherical geometry. *Journal of the Atmospheric Sciences* **65** (2), 655–660.

Bretherton, Christopher S & Sobel, Adam H 2003 The gill model and the weak temperature gradient approximation. *Journal of the atmospheric sciences* **60** (2), 451–460.

Chao, Winston C 1987 On the origin of the tropical intraseasonal oscillation. *Journal of the atmospheric sciences* **44** (15), 1940–1949.

Chao, Winston C & Chen, Baode 1999 Approximate co-location of precipitation and low-level westerlies in tropical monthly means. In *Preprint, Eighth Conf. on Climate Variations, Denver, CO, Ame. Meteor. Soc*, pp. 195–198.

Chelton, Dudley B, Deszoeke, Roland A, Schlax, Michael G, El Naggar, Karim & Siwertz, Nicolas 1998 Geographical variability of the first baroclinic rossby radius of deformation. *Journal of Physical Oceanography* **28** (3), 433–460.

Covey, Curt & Schubert, Gerald 1982 Planetary-scale waves in the venus atmosphere. *Journal of Atmospheric Sciences* **39** (11), 2397–2413.

DallaSanta, Kevin, Gerber, Edwin P & Toohey, Matthew 2019 The circulation response to volcanic eruptions: The key roles of stratospheric warming and eddy interactions. *Journal of Climate* **32** (4), 1101–1120.

De-Leon, Yair & Paldor, Nathan 2011 Zonally propagating wave solutions of Laplace Tidal Equations in a baroclinic ocean of an aqua-planet. *Tellus A* **63** (2), 348–353.

De-Leon, Yair, Paldor, Nathan & Garfinkel, Chaim I 2020 Barotropic modes, baroclinic modes and equivalent depths in the atmosphere. *Quarterly Journal of the Royal Meteorological Society* **146** (730), 2096–2115.

Del Genio, Anthony D & Rossow, William B 1990 Planetary-scale waves and the cyclic nature of cloud top dynamics on venus. *Journal of Atmospheric Sciences* **47** (3), 293–318.

Ángel F. Adames & Wallace, John M. 2014 Three-dimensional structure and evolution of the vertical velocity and divergence fields in the mjo. *Journal of the Atmospheric Sciences* **71** (12), 4661 – 4681.

Fritts, David C & Alexander, M Joan 2003 Gravity wave dynamics and effects in the middle atmosphere. *Reviews of geophysics* **41** (1).

Garfinkel, Chaim I, Shamir, Ofer, Fouxon, Itzhak & Paldor, Nathan 2021 Tropical background and wave spectra: Contribution of wave–wave interactions in a moderately nonlinear turbulent flow. *Journal of the Atmospheric Sciences* **78** (6), 1773–1789.

Garfinkel, I. Chaim, Fouxon, Itzhak, Shamir, Ofer & Paldor, Nathan 2017 Classification of eastward propagating waves on the spherical earth. *Quarterly Journal of the Royal Meteorological Society, In Press* .

Gill, Adrian E 1980 Some simple solutions for heat-induced tropical circulation. *Quarterly Journal of the Royal Meteorological Society* **106** (449), 447–462.

Holton, James R & Colton, Donald E 1972 A diagnostic study of the vorticity balance at 200 mb in the tropics during the northern summer. *Journal of the Atmospheric Sciences* **29** (6), 1124–1128.

Hoskins, Brian J & Ambrizzi, Tercio 1993 Rossby wave propagation on a realistic longitudinally varying flow. *Journal of Atmospheric Sciences* **50** (12), 1661–1671.

Hoskins, Brian J & Karoly, David J 1981 The steady linear response of a spherical atmosphere to thermal and orographic forcing. *Journal of the Atmospheric Sciences* **38** (6), 1179–1196.

Hough, Sydney Samuel 1897 V. on the application of harmonic analysis to the dynamical theory of the tides.—part i. on laplace's "oscillations of the first species" and on the dynamics of ocean currents. *Philosophical Transactions of the Royal Society of London. Series A, Containing Papers of a Mathematical or Physical Character* **189**, 201–257.

Hough, Sydney Samuel 1898 V. on the application of harmonic analysis to the dynamical theory of the tides.—part ii. on the general integration of laplace's dynamical equations. *Philosophical Transactions of the Royal Society of London. Series A, Containing Papers of a Mathematical or Physical Character* **191**, 139–185.

Kacimi, Abderrahim & Khouider, Boualem 2018 The transient response to an equatorial heat source and its convergence to steady state: implications for mjo theory. *Climate dynamics* **50** (9-10), 3315–3330.

Lin, Jia-Lin, Mapes, Brian E & Han, Weiqing 2008 What are the sources of mechanical damping in matsuno–gill-type models? *Journal of Climate* **21** (2), 165–179.

Longuet-Higgins, Michael Selwyn 1968 The eigenfunctions of laplace's tidal equation over a sphere. *Philosophical Transactions of the Royal Society of London. Series A, Mathematical and Physical Sciences* **262** (1132), 511–607.

Lutsko, Nicholas J 2018 The response of an idealized atmosphere to localized tropical heating: Superrotation and the breakdown of linear theory. *Journal of the Atmospheric Sciences* **75** (1), 3–20.

Majda, Andrew J & Stechmann, Samuel N 2009 The skeleton of tropical intraseasonal oscillations. *Proceedings of the National Academy of Sciences* **106** (21), 8417–8422.

Matsuno, Taroh 1966 Quasi-geostrophic motions in the equatorial area. *J. Meteor. Soc. Japan* **44** (1), 25–43.

Mitchell, Jonathan L, Ádámkovics, Máté, Caballero, Rodrigo & Turtle, Elizabeth P 2011 Locally enhanced precipitation organized by planetary-scale waves on titan. *Nature Geoscience* **4** (9), 589–592.

Müller-Wodarg, Ingo, Griffith, Caitlin A, Lellouch, Emmanuel & Cravens, Thomas E 2014 *Titan: Interior, surface, atmosphere, and space environment*, , vol. 14. Cambridge University Press.

Neelin, J David 1988 A simple model for surface stress and low-level flow in the tropical atmosphere driven by prescribed heating. *Quarterly Journal of the Royal Meteorological Society* **114** (481), 747–770.

Paldor, Nathan, De-Leon, Yair & Shamir, Ofer 2013 Planetary (Rossby) waves and inertia–gravity (Poincaré) waves in a barotropic ocean over a sphere. *Journal of Fluid Mechanics* **726**, 123–136.

Paldor, Nathan, Fouxon, Itzhak, Shamir, Ofer & Garfinkel, Chaim I 2018 The mixed rossby–gravity wave on the spherical earth. *Quarterly Journal of the Royal Meteorological Society* **144** (715), 1820–1830.

Peralta, J., Navarro, T., Vun, C. W., Sánchez-Lavega, A., McGouldrick, K., Horinouchi, T., Imamura, T., Hueso, R., Boyd, J. P., Schubert, G., Kouyama, T., Satoh, T., Iwagami, N., Young, E. F., Bullock, M. A., Machado, P., Lee, Y. J., Limaye, S. S., Nakamura, M., Tellmann, S., Wesley, A. & Miles, P. 2020 A long-lived sharp disruption on the lower clouds of venus. *Geophysical Research Letters* **47** (11), e2020GL087221, e2020GL087221 10.1029/2020GL087221, arXiv: https://agupubs.onlinelibrary.wiley.com/doi/pdf/10.1029/2020GL087221.

Romps, David M 2014 Rayleigh damping in the free troposphere. *Journal of the Atmospheric Sciences* **71** (2), 553–565.

Sardeshmukh, Prashant D & Held, Isaac M 1984 The vorticity balance in the tropical upper troposphere of a general circulation model. *Journal of the atmospheric sciences* **41** (5), 768–778.

Shamir, Ofer, Garfinkel, Chaim I, Adam, Ori & Paldor, Nathan 2021*a* A note on the power distribution between symmetric and antisymmetric components of the tropical brightness temperature spectrum in the wavenumber–frequency plane. *Journal of the Atmospheric Sciences* **78** (11), 3473–3476.

Shamir, Ofer, Schwartz, Chen, Garfinkel, Chaim I & Paldor, Nathan 2021*b* The power distribution between symmetric and antisymmetric components of the tropical wavenumber–frequency spectrum. *Journal of the Atmospheric Sciences* **78** (6), 1983–1998.

Showman, Adam P & Polvani, Lorenzo M 2010 The matsuno-gill model and equatorial superrotation. *Geophysical Research Letters* **37** (18).

Smith, Michael D, Gierasch, Peter J & Schinder, Paul J 1992 A global traveling wave on venus. *Science* **256** (5057), 652–655.

Sobel, Adam & Maloney, Eric 2012 An idealized semi-empirical framework for modeling the madden–julian oscillation. *Journal of the Atmospheric Sciences* **69** (5), 1691–1705.

Svedhem, Håkan, Titov, Dmitry V, Taylor, Fredric W & Witasse, Olivier 2007 Venus as a more earth-like planet. *Nature* **450** (7170), 629–632.

Toohey, Matthew, Krüger, Kirstin, Bittner, Matthias, Timmreck, Claudia & Schmidt, Hauke 2014 The impact of volcanic aerosol on the northern hemisphere stratospheric polar vortex: mechanisms and sensitivity to forcing structure. *Atmospheric Chemistry and Physics* **14** (23), 13063–13079.

Trefethen, Lloyd N 2000 *Spectral methods in MATLAB*, , vol. 10. Siam.

Wilka, Catherine, Solomon, Susan, Cronin, Timothy W, Kinnison, Doug & Garcia, Rolando 2021 Atmospheric chemistry signatures of an equatorially symmetric matsuno–gill circulation pattern. *Journal of the Atmospheric Sciences* **78** (1), 107–116.

Yamamoto, Masaru 2019 Equatorial kelvin-like waves on slowly rotating and/or small-sized spheres: Application to venus and titan. *Icarus* **322**, 103–113.

Zhang, C., Adames, Á. F., Khouider, B., Wang, B. & Yang, D. 2020 Four theories of the madden-julian oscillation. *Reviews of Geophysics* **58** (3), e2019RG000685, e2019RG000685 2019RG000685, arXiv: https://agupubs.onlinelibrary.wiley.com/doi/pdf/10.1029/2019RG000685.

Zhu, Jinshuang, Liu, Yudi, Xie, Ruiqing & Chang, Haijie 2018 A comparative analysis of the impacts of two types of el niño on the central and eastern pacific itcz. *Atmosphere* **9** (7), 266.